

Predicting the Long-Term Behavior of a Micro-Solar Power System

JAEIN JEONG, Cisco Systems

DAVID CULLER, University of California, Berkeley

Micro-solar power system design is challenging because it must address long-term system behavior under highly variable solar energy conditions and consider a large space of design options. Several micro-solar power systems and models have been made, validating particular points in the whole design space. We provide a general architecture of micro-solar power systems—comprising key components and interconnections among the components—and formalize each component in an analytical or empirical model of its behavior. To model the variability of solar energy, we provide three solar radiation models, depending on the degree of information available: an astronomical model for ideal conditions, an obstructed astronomical model for estimating solar radiation under the presence of shadows and obstructions, and a weather-effect model for estimating solar radiation under weather variation. Our solar radiation models are validated with a concrete design, the HydroWatch node, thus achieving small deviation from the long-term measurement. They can be used in combination with other micro-solar system models to improve the utility of the load and estimate the behavior of micro-solar power systems more accurately. Thus, our solar radiation models provide more accurate estimations of solar radiation and close the loop for micro-solar power system modeling.

Categories and Subject Descriptors: C.5.m [Computer System Implementations]: Miscellaneous; D.4.7 [Operating Systems]: Organization and Design—*Real-time systems and embedded systems*; I.6.3 [Simulation and Modeling]: Applications; I.6.4 [Simulation and Modeling]: Model Validation and Analysis; I.6.5 [Simulation and Modeling]: Model Development—*Modeling methodologies*

General Terms: Algorithms, Design, Experimentation, Measurement, Verification

Additional Key Words and Phrases: Micro-solar power system, radiation models, obstructions, weather effects, validation

ACM Reference Format:

Jeong, J. and Culler, D. 2012. Predicting the long-term behavior of a micro-solar power system. ACM Trans. Embed. Comput. Syst. 11, 2, Article 35 (July 2012), 38 pages.
DOI = 10.1145/2220336.2220347 <http://doi.acm.org/10.1145/2220336.2220347>

1. INTRODUCTION

Autonomous long-term monitoring is one of the visions of wireless sensor networks (WSNs), and a key limiting factor is the ratio of power consumption to energy supply. Non-rechargeable batteries on which most sensor network applications run, are not suitable for long-term monitoring due to their finite capacity [Kim 2007; Szewczyk et al. 2004; Tolle et al. 2005]. Power-saving solutions at the application level [Madden et al. 2002; Nath et al. 2004; Pradhan et al. 2002; Scaglione and Servetto 2002] and the network

This work was supported by the Defense Advanced Research Projects Agency (grant F33615-01-C-1895), the Keck Foundation (grant HydroWatch Center), and the National Science Foundation (grant 0435454 “NeTS-NR” and 0454432 “CNS-CRI”). It was also supported by the Korea Foundation for Advanced Studies Fellowship, as well as generous gifts from the Hewlett-Packard Company, Intel Research, and California MICRO.

Authors’ addresses: J. Jeong, Cisco Systems, San Jose, CA; email: jajeong@cisco.com; D. Culler, Computer Science Division, UC Berkeley, Berkeley, CA; email: culler@eecs.berkeley.edu.

Permission to make digital or hard copies of part or all of this work for personal or classroom use is granted without fee provided that copies are not made or distributed for profit or commercial advantage and that copies show this notice on the first page or initial screen of a display along with the full citation. Copyrights for components of this work owned by others than ACM must be honored. Abstracting with credit is permitted. To copy otherwise, to republish, to post on servers, to redistribute to lists, or to use any component of this work in other works requires prior specific permission and/or a fee. Permissions may be requested from the Publications Dept., ACM, Inc., 2 Penn Plaza, Suite 701, New York, NY 10121-0701, USA, fax +1 (212) 869-0481, or permissions@acm.org.

© 2012 ACM 1539-9087/2012/07-ART35 \$15.00

DOI 10.1145/2220336.2220347 <http://doi.acm.org/10.1145/2220336.2220347>

level [Chen et al. 2001; Dust Networks 2006; Polastre et al. 2004; Ye et al. 2004, 2006; Zhang et al. 2007] are not viable options, because they are still susceptible to limited amounts of energy, although reduced power consumption improves deployment lifetime. Renewable energy sources, such as solar radiation, vibration, human power, and air flow, can be used to address this problem, as a renewable-energy-powered node can potentially run for a long period of time without requiring the replacement of the battery. Among these renewable energy sources, solar energy is the most promising for an outdoor, wireless sensor network application. It has higher power density than other renewable energy sources, allowing a sensor node to collect sufficient energy with a small form factor.

Realizing the opportunity for perpetual operation, several micro-solar power systems have been made [Corke et al. 2007; Dutta et al. 2006; Jiang et al. 2005; Park and Chou 2006; Raghunathan et al. 2005; Simjee and Chou 2006; Zhang et al. 2004]. While these implementations demonstrated that building a micro-solar power system is possible, they address only particular points in the design space of micro-solar power systems, rather than providing a general model. These implementations do not provide guidance when they are placed in a setting different from their target environment or if a different configuration of micro-solar power system is used. In order to explore possible choices in the design space of micro-solar power systems, a general model is needed. A number of previous models have been made that predict or schedule system behavior with periodic measurement of micro-solar systems [Jiang et al. 2005; Kansal et al. 2004, 2007; Moser et al. 2006b, 2007; Nahapetian et al. 2007; Piorno et al. 2009; Raghunathan et al. 2005; Sorber et al. 2007; Vigorito et al. 2007]. While these approaches are useful for optimizing the utility of a node in the ongoing deployment, they have a limitation for predicting the long-term behavior in varying deployment conditions prior to the deployment, because they predict the system behavior using ongoing measurements of system status and solar radiation, rather than modeling entire components of a micro-solar power system using well-formed analytical models.

The goal of this article is to provide a generic model of micro-solar power systems and ways to accurately estimate the energy-flow of the system in a realistic environment. To enable energy flow estimation for micro-solar power systems, we present three solar radiation models, each of which can achieve higher accuracy with additional data. As a basis of the solar radiation model, we provide an astronomical model, which can estimate the solar radiation in an ideal condition very well with no obstructions or weather effects.

To improve the estimation accuracy under obstructions, we extended the astronomical model into an obstructed astronomical model. The obstructed astronomical model calculates obstruction patterns using a small sample of solar profile measurements and refines the estimation from the astronomical model. The obstructed astronomical model predicts the solar profile on a clear day and achieves an average 30% deviation from the measurement on a five-month long experiment, even under the weather variations of a rainy season. To further improve the estimation accuracy of the obstructed astronomical model, we extended it into a weather-effect model by maintaining the history of weather metrics for a small duration. The weather-effect model using cloud conditions achieves an average 7% deviation from the measurement. Another advantage of our radiation models is that they are general purpose and are widely applicable, as long as a few samples of local solar radiation profiles are measured and weather reports from the nearest weather stations are provided.

The solar radiation predictions of our models can be used in combination with other micro-solar power system models to adjust load duty cycles more aggressively or estimate battery lifetime more accurately, compared to cases in which no prediction of solar radiation is provided. By providing more accurate estimations of solar radiation,

which has thus far been estimated by very coarse-grained or inaccurate estimators, we can improve the utility of the load and estimate the behavior of micro-solar power systems more accurately. Thus, our models provide more accurate estimations of solar radiation and close the loop for micro-solar power system modeling.

The contributions of this article are as follows. (i) We provide an architecture of micro-solar power systems; (ii) we develop two refinements of the astronomical solar radiation model that can estimate solar radiation, even in the presence of obstructions and weather effects; (iii) we validate the two refined radiation models by comparing solar energy estimates with empirical results in a realistic environment.

This article is organized into six sections. Section 2 compares outdoor solar energy with other types of energy sources and identifies it as a feasible solution for powering outdoor wireless sensor network applications. It then provides a background overview of solar energy harvesting in the domain of wireless sensor networks. Section 3 presents an architecture of micro-solar power systems, describing the characteristics of its key components and the relationships among its components. Section 4 develops and evaluates the obstructed astronomical model that refines the solar radiation profile estimate from the astronomical model with small samples of local solar radiation measurements. Section 5 develops the weather-effect model that estimates solar radiation under weather variations using publicly available data and evaluates whether the model can predict variation of solar radiation with sufficient accuracy. Finally, Section 6 concludes this article.

2. BACKGROUND

2.1 Wireless Sensor Networks and Energy Sources

A wireless sensor node can be categorized into either *non-rechargeable battery powered*, *wire powered*, or *renewable energy powered* depending on the characteristic of the energy sources. A non-rechargeable battery is the most commonly used, because it is relatively inexpensive and the sensor node can be placed anywhere, but the lifetime of a battery-powered node is limited by the finite capacity of the non-rechargeable battery [Kim 2007; Szewczyk et al. 2004]. Another way to supply energy to sensor nodes is through a *wired back-channel*. Many wireless sensor network testbeds have a wired back-channel for maintenance purposes, such as reprogramming and data downloading, but they also utilize this to power the sensor nodes [Handziski et al. 2006; Polastre et al. 2005; Werner-Allen et al. 2005]. While wire power makes it easy to maintain a testbed, it is limited to where a wiring is available. In an outdoor deployment, wire power may not be available, and making such devices weather proof or wildlife safe can add huge costs and complexity. It is the limiter in outdoor testbeds. A *renewable energy-powered* node runs on a renewable energy source, such as solar radiation, vibrations, human power, or air flow, and is expected to run for a long period of time without requiring the replacement of the battery. From among the various renewable energy sources, we focus on outdoor solar energy in this article for two reasons. First, outdoor solar energy has higher power density than other renewable energy sources, and this allows us to build a solar energy harvesting system with a small form factor; second, the commercial availability of solar panels allows us to focus on the energy harvesting system from the perspective of computer science, which consists of synthesis, modeling, and analysis, without the need to build the energy harvesting material itself.

2.2 Prior Work on Micro-Solar Power Systems

Recognizing the possibility of long-term autonomous operation, several implementations have been made: ZebraNet [Zhang et al. 2004], Prometheus [Jiang et al. 2005],

Table I. Comparison of Micro-Solar Power System Platforms

Examples	Energy Storage	Solar Panel Operating Point	Goal
Heliomote Fleck	NiMH	Depends on battery voltage	Simple charging mechanism
ZebraNet	Li+	Fixed range set by hardware	Storage efficiency
Prometheus Trio	Supercap and Li+	Operating range set by software	Flexible configuration
Everlast	Supercap	MPPT controlled by software	Storage lifetime and solar panel operating point
AmbiMax	Supercap and Li+	MPPT controlled by hardware	Storage lifetime and solar panel operating point

Heliomote [Raghunathan et al. 2005], Everlast [Simjee and Chou 2006], Trio [Dutta et al. 2006], AmbiMax [Park and Chou 2006], and Fleck [Corke et al. 2007]. While these implementations demonstrate that building a sensornet system with solar energy harvesting is possible, they address only particular points in the design space of micro-solar power systems, rather than providing a general model (see Table I). These implementations do not provide guidance when they are placed in a setting different from their target environment or if a different configuration of micro-solar power system is used. In order to explore possible choices in the design space of micro-solar power systems, a general model is needed.

2.2.1 Sensor Network Models Related to Micro-Solar Power Systems. Some of the previous research has shown that duty-cycle [Jiang et al. 2005; Kansal et al. 2004, 2007; Nahapetian et al. 2007; Raghunathan et al. 2005; Vigorito et al. 2007], task-scheduling [Moser et al. 2006a], or energy-harvesting-aware programming language [Sorber et al. 2007] could be adjusted dynamically, depending on the environment, in order to achieve higher utilization and meet scheduling deadlines. Jiang et al. [2005] showed a simple duty-cycling scheme, but they provided just a proof of concept without elaborating upon the formal relation between the desired duty-cycle rate and the corresponding system parameters. Kansal et al. [2004] proposed a bound rule for sustainable operation of energy-harvested nodes, showing that a Heliomote node on their experiment setting meets the rule and can operate sustainably. Moser et al. [2006b] showed an energy-aware deadline-scheduling algorithm, but it has a limitation in that it assumes ideal storage, and the results are shown only in simulation with no consideration of realistic energy-harvesting devices. Kansal et al. [2007] and Vigorito et al. [2007] proposed dynamic duty-cycling algorithms that optimized the duty cycle of the load, depending on energy availability by using linear programming or linear quadratic tracking. While they work well as online duty cycle optimizers, they are limited when used as long-term estimation tools by themselves: when calculating the system status at each time step, they take the solar panel output or battery level externally instead of modeling it, requiring measurements or estimations from other tools.

There are several sensor network simulators that can estimate power consumption of sensor nodes. PowerTOSSIM [Shnayder et al. 2004], SensorSim [Park et al. 2000, 2001], Prowler [Simon et al. 2003], SENS [Sundresh et al. 2004] and AEON [Landsiedel et al. 2005] are such examples. These simulators are similar to each other in that they execute a sensor network application and estimate power consumption based on the prerecorded energy consumption profile of primitive operations on the target, but they differ in simulation platform, target sensor node platform, source base,

and extensibility. When choosing a sensor network power simulator, we are interested in two factors: reality and extensibility. For reality, we prefer a simulator that takes an actual application program code and simulates the corresponding power consumption (e.g., PowerTOSSIM and AEON). For extensibility, we prefer a simulator that is based on a generic sensor platform (e.g., SensorSIM, Prowler, and SENS). Such a simulator could be easily used for evolving sensor network platforms by changing the platform-specific parameters.

A couple of research groups proposed a way to estimate the battery capacity or lifetime for WSNs [Park et al. 2000, 2001; Varshney et al. 2007]. Although these are built to model the discharge rate of a non-rechargeable battery, they can be extended for micro-solar power systems by considering the charging profile of the battery, as well as the discharging profile. These battery simulators vary in terms of their functions and complexity.

2.2.2 Solar Radiation Models. As a way of estimating solar radiation, a software suite called Meteororm [Meteororm 2003] can be used. Its meteorological database covers over 30 years of solar radiation measurements from a number of locations around the world. If a location is not in the database, Meteororm estimates its approximate solar radiation based on its geographic characteristics (latitude, longitude, and altitude) and matches it to the data of previously known locations. Meteororm provides different time granularity (month, day, hour) when it estimates solar radiation. Depending on the responsiveness of the application, solar radiation estimates of suitable time granularity can be used. One difference between Meteororm and our work is that Meteororm provides only the statistics of solar radiation, whereas our model can estimate the whole system behavior, as well as the solar radiation. Another difference is that Meteororm estimates solar radiation only for a representative condition, whereas our model can predict different solar radiations in a location due to different shading conditions.

With an astronomical model, we estimate the solar radiation using parameters that affect the angle between the sunlight and the solar panel. When the angle of sunlight from the normal to the solar panel is Θ , the effective sunlight that shines on the solar panel is proportional to $\cos \Theta$ [Dave et al. 1975]. The angle Θ depends on solar-panel inclination θ_p , panel orientation ϕ_p , latitude L , time of the day t , and day of the year n .

The astronomical model estimates the solar radiation relatively accurately at an ideal condition in which the solar panel is exposed to the sun in clear weather without any obstructions. On an overcast day, however, the estimation of the astronomical model deviates far from the reality. In the atmospheric science community, weather metrics, such as atmospheric turbidity [Cannon and Hulstrom 1988; Peterson et al. 1978; Robinson and Valente 1982] and horizontal visibility [Peterson et al. 1978], are known to have a high correlation with solar radiation under weather variations. We can estimate solar radiation under weather effects using these weather metrics, even though these metrics are designed as a measure of air pollution or air traffic safety.

2.2.3 Relation to Macro-Solar Power Systems. There are many calculators for macro-solar power systems (National Renewable Energy Laboratory¹; FindSolar²; Iowa

¹PVWATTS: A Performance Calculator for Grid-Connected PV Systems.
http://rredc.nrel.gov/solar/codes_algs/PVWATTS.

²Connecting You to Renewable Energy Professionals. <http://findsolar.com>.

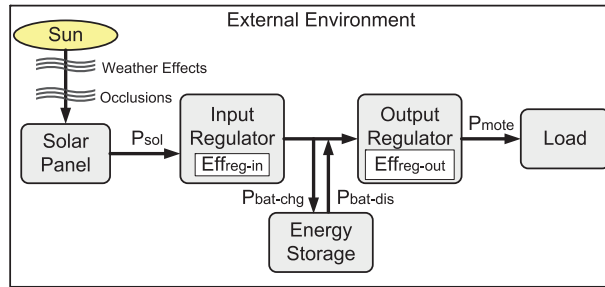


Fig. 1. Model for a solar-powered sensor system.

Energy Center³; Sunpower⁴; California Solar Initiative⁵; Weather Underground⁶). Concepts from these tools can be applied to micro-solar power systems: they compose a system as a collection of several components and their interconnections, and they estimate solar radiation using an astronomical model. However, they are not suitable for modeling the dynamics of micro-solar power systems due to the following reasons. First, each component is represented as a single number, rather than a function or a curve. This approach may predict the average or maximum performance but cannot predict the varying performance with different operating points. Second, due to economic reasons, these macro-solar tools assume that energy surpluses are sold to the grid rather than accumulated into energy storage. However, because micro-solar power systems are often placed where grid power is not available, micro-solar systems generally require energy storage, breaking the assumption used in these macro-solar tools.

3. ARCHITECTURE OF MICRO-SOLAR POWER SYSTEMS

3.1 Components of Micro-Solar Power Systems

In general, any solar-powered system consists of the following six components: *external environment*, *solar panel*, *input regulator*, *energy storage*, *output regulator* and *load* (see Figure 1). The solar energy from the environment is collected by the solar collector and is made available for the operation of the load. The energy storage is used to buffer the varying energy income and distribute it to the load throughout the duration. The input regulator can be used to adjust the mismatch between the operating range of the solar panel and the energy storage, while the output regulator is used to shape the operating range of the energy storage to that of the load. The design decisions for each component will dictate the energy flow between them and the overall behavior of the system. In the rest of this section, we describe the architecture of a micro-solar power system in terms of the energy flow of each component.

3.1.1 External Environment. The amount of solar radiation $P_{solar-in}$ depends on the environment, and it places an upper bound on the maximum energy output of the solar collector P_{sol} . We describe three ways to estimate solar radiation: (a) an astronomical method, (b) an astronomical method with local enhancements, and (c) an astronomical method with history of weather effects.

³Solar Data for Iowa Locations. <http://www.energy.iastate.edu/renewable/solar/calculator>.

⁴Sunpower Solar Calculator.

<http://www.sunpowercorp.com/For-Homes/How-To-Buy/Solar-Calculator.aspx>.

⁵Incentive Calculator. <http://www.csi-epbb.com>.

⁶Solar Calculator. <http://www.wunderground.com/calculators/solar.html>.

With an astronomical model, we estimate the solar radiation using the parameters that affect the angle between the sunlight and the solar panel. According to Dave et al. [1975], the effective sunlight that shines on the solar panel is proportional to $\cos \Theta$ when the angle of sunlight from the normal to the solar panel is Θ . The angle Θ depends on solar panel inclination θ_p , panel orientation ϕ_p , latitude L , time of the day t , and day of the year n .

$$\begin{aligned}
 \cos \Theta &= \cos \theta_p \cdot \cos \theta_s + \sin \theta_p \cdot \sin \theta_s \cdot \cos(\phi_p - \phi_s); \\
 \cos \theta_s &= \sin \delta \cdot \sin L + \cos \delta \cdot \cos L \cdot \cos h; \\
 \sin \phi_s &= -\cos \delta \cdot \sin h / \sin \theta_s; \\
 x &= 2\pi n / 365; \\
 h &= 15(t - 12); \\
 \delta &= 0.302 - 22.93 \cos x - 0.229 \cos 2x - 0.243 \cos 3x \\
 &\quad + 3.851 \sin x + 0.002 \sin 2x - 0.055 \sin 3x.
 \end{aligned} \tag{1}$$

The astronomical model works well on a clear day and can be used without knowledge of the deployment site, but its estimation error can be high due to obstructions from local objects, such as trees and buildings or weather effects. With a measurement of local obstructions and history of weather effects, the astronomical model can be refined for obstructions and weather effects. These refined radiation models will be discussed in Sections 4 and 5.

Note that the astronomical model itself is not our contribution but is presented to set a basis for the obstructed astronomical model and the weather-effect model. Using the astronomical model allows these models to predict time-varying energy availability. As previously mentioned, the effects from weather, terrain, and air quality are not modeled by the astronomical model. However, these effects can be modeled with the obstructed astronomical model and weather-effect model by using measurements of weather, local obstructions, and air quality.

3.1.2 Solar Collector. Solar energy from the environment is converted to electric energy by the solar collector, which includes a solar panel and a regulator. The amount of solar power out of the solar collector P_{sol} is determined by the following factors: (1) solar-panel characteristics, (2) solar radiation, and (3) the operating point of the solar-panel. A given panel is characterized by its IV curve and, in particular, three points: the open-circuit voltage (V_{oc}), short-circuit current (I_{sc}), and maximum power point (MPP). The solar-panel IV characteristic also depends on the radiation condition. As the solar irradiance increases or decreases, the IV curve moves outwards or inwards. Thus, a solar panel can be described as a sequence of IV curves, with each IV curve corresponding to a particular solar irradiance condition (see Figure 2). The operating point of the IV curve is determined by the load experienced at the panel, which is determined by the input regulator, storage facility, and downstream load. While the output of a solar panel is mostly determined by solar-panel characteristics, solar radiation, and operating point, the degradation of a panel also needs to be considered for a long-term estimation. It is known that the output power of a solar panel exposed to the sunlight degrades less than 1% per year with varying rates, depending on the material used [Osterwald et al. 2002].

3.1.3 Input-Power Conditioning. In a micro-solar power system, an input regulator can be used to set the specific operating point of the solar panel to meet the operational constraints of the particular energy storage using voltage limits, current limits, and charge duration. While matching the operating points of the solar panel and energy storage is an advantage of using an input regulator, the sub-unity efficiency of the

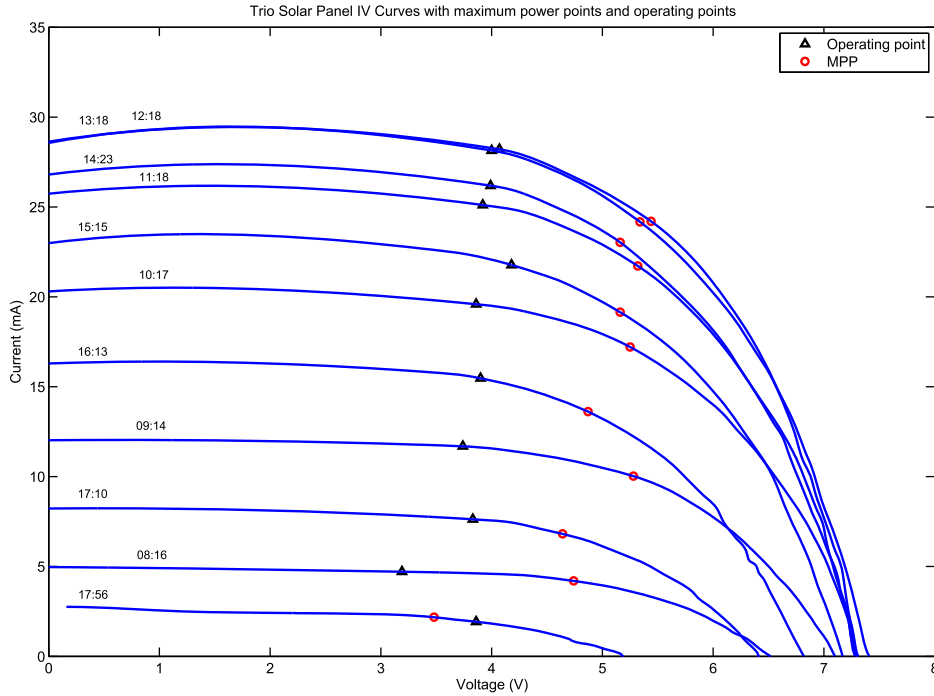


Fig. 2. A series of IV characteristics for a poly-crystalline solar panel. The dimension of this panel is 67mm x 37mm, and its rated current and voltage are 30mA and 6.7V, respectively. The operating point on each IV curve corresponds to the voltage and the current of the solar panel that is being used in a Trio node.

input regulator is a drawback. The efficiency of an input regulator $\text{Eff}_{\text{reg-in}}$ is 50% to 80%, depending on the part being used. Thus, analysis of the possible gain of the operating point matching against the inefficiency of the input regulator should be made before it is used in a micro-solar power system.

3.1.4 Energy Storage. Energy storage is the group of storage elements used to buffer the energy coming from the solar collector and deliver it to the mote in a predictable fashion. A wide range of battery configurations and chemistries, as well as supercapacitors, can be used with differing operating voltages, charge algorithms, and complexities. The portion of energy transferred into the energy storage during the day and discharged during the night incurs an additional round-trip transfer efficiency, Eff_{bat} , of about 66%⁷ for NiMH chemistries. The capacity of the battery determines not only the potential lifetime in darkness but also how much energy can be harvested while the sun shines.

3.1.5 Output-Power Conditioning. In a micro-solar power system, an output regulator can be used to condition the output of the energy storage to meet the operational voltage range of the load. An output regulator has a wider operating input voltage than the load, and it shapes the output voltage of the energy storage to fit within the operating voltage of the load most of the time. Another reason to use an output regulator is to provide a constant supply of voltage for sensing applications. Having an output regulator makes the supply of voltage to the sensor node near-constant, which can

⁷With charging rate 0.1C/hour, where C is the capacity of the battery.

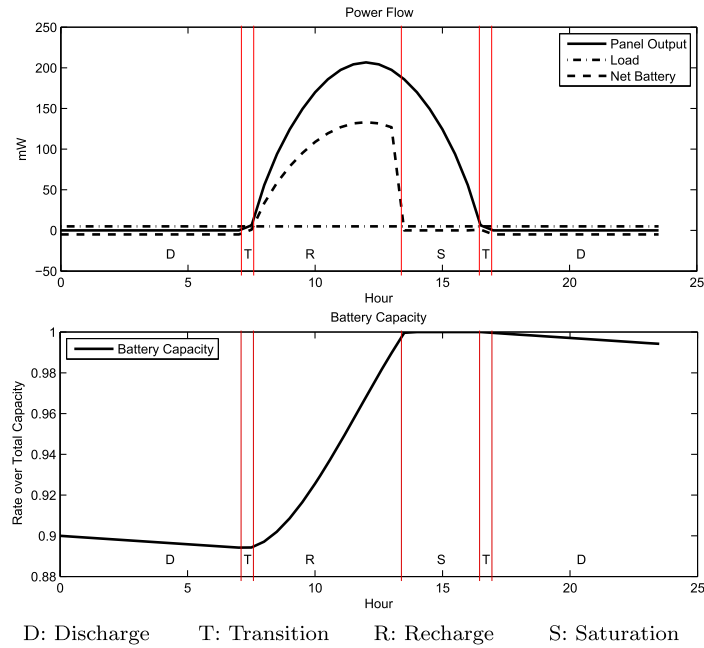


Fig. 3. Energy flow and daily phases in our micro-solar model.

improve the quality of the ADC readings. The output regulator is characterized by its efficiency, $\text{Eff}_{\text{reg-out}}$, and in particular, by its efficiency at two very different operating points: 10s of micro-watts (most of the time) and 10s of milliwatts (during short active periods). For a typical bimodal P_{mote} , an effective efficiency of 50% or less is expected.

3.1.6 Load. The sensor node (mote) is the end consumer of energy in our micro-solar power system. The amount of energy a mote consumes (P_{cons}) can be modeled by two main causes: radio communication and sensing. Since a mote draws a much higher current when its radio chip is awake, radio duty-cycling is commonly used as a technique to lower the energy consumption of a mote. Power savings for the sensing device can be achieved in a similar way. A mote's current consumption rate I_{est} can be estimated with the following formula if the current consumption rates for the sleep state and the active state (I_{sleep} and I_{awake}) are known: $I_{\text{est}} = R \cdot I_{\text{awake}} + (1 - R) \cdot I_{\text{sleep}}$.

With duty-cycling, the power consumption of the load itself looks like the average value, but it can be more than the average value when the load is connected to the rest of the system through the output regulator. Typically, the efficiency of an output regulator varies depending on the load current. For more accurate modeling, the efficiency of the output regulator should be adjusted according to the operating modes and the frequency of the load.

3.2 Modeling Interconnection

The behavior of the system has a roughly daily pattern; generally, the daily power cycle has five phases, as illustrated in Figure 3. From sundown to sun up, the battery *discharges*, supplying the device load. As the panel is initially illuminated, a *transition period* occurs during which the battery provides only a portion of the device load. With sufficient illumination, the panel supports the entire load and delivers charge into the battery. If this *recharge period* is sustained sufficiently long, the battery becomes fully

charged and the system operates in *saturation*, shunting power. Eventually, a dusk transition occurs similar to dawn. The efficiency coefficients dictate the net change in battery capacity over the daily cycle, given the starting capacity, supply power, and demand power. Our sizing guideline assumed that the recharge period would need to be no more than half an hour, possibly distributed throughout the day. Saturation merely preserves capacity. Of course, a series of overcast days may result in a progressive drop in battery capacity, which would then increase the recharge duration when the weather clears. In the micro-solar setting, given the ratio of mote load to typical battery capacities, it is even reasonable to consider design points that absorb entire seasonal variations in weather patterns.

In the *discharge period*, there is no solar energy available, and the battery is discharged to run the load. If we assume constant load consumption, we can formulate the condition of each component of the micro-solar power system as follows.

$$P_{sol} = 0, P_{bat-chg} = 0, P_{bat-dis} > 0, P_{mote} = \text{const}; \quad (2)$$

$$P_{mote} = P_{bat-dis} \cdot \text{Eff}_{reg-out}. \quad (3)$$

In the *transition period*, there is solar radiation, but it is not high enough to charge the battery. Since the energy to run the load comes from both the solar radiation and the battery discharge, the following relationship can hold.

$$P_{sol} > 0, P_{bat-chg} = 0, P_{bat-dis} > 0, P_{mote} = \text{const}; \quad (4)$$

$$P_{mote} = (P_{sol} \cdot \text{Eff}_{reg-in} + P_{bat-dis}) \cdot \text{Eff}_{reg-out}. \quad (5)$$

This relationship can be further reduced when the micro-solar power system has an input regulator with $\text{Eff}_{reg-in} = 1$.

$$P_{mote} = (P_{sol} + P_{bat-dis}) \cdot \text{Eff}_{reg-out}. \quad (6)$$

In Equations (5) and (6), each power entity is assumed to be an average value over a discrete time interval. Here, we assume that we use a rechargeable battery as energy storage. When the power from the solar panel is not sufficient for operation of the mote, the mote draws current from the battery, incurring a battery discharge. The addition operations in the equations describe this situation.

In the *recharge period*, the solar radiation is sufficiently high, and the energy to run the mote comes from solar radiation. At the same time, the rest of the solar radiation is stored in the energy storage. Then, the following relationship can hold among each component.

$$P_{sol} > 0, P_{bat-chg} > 0, P_{bat-dis} = 0, P_{mote} = \text{const}; \quad (7)$$

$$P_{sol} \cdot \text{Eff}_{reg-in} = P_{bat-chg} + P_{mote} / \text{Eff}_{reg-out}. \quad (8)$$

In the *saturation period*, the solar radiation is sufficiently high, but the energy storage is fully charged. The energy to run the load comes from the solar radiation with the battery not being charged nor being discharged, and the rest of energy from solar radiation is shunted.

$$P_{sol} > 0, P_{bat-chg} = 0, P_{bat-dis} = 0, P_{mote} = \text{const}; \quad (9)$$

$$P_{sol} \cdot \text{Eff}_{reg-in} = P_{shunted} + P_{mote} / \text{Eff}_{reg-out}. \quad (10)$$

Using these relations, the status of a micro-solar power system can be simulated over time. At each time interval, the simulator estimates an energy increment $P_{bat-chg}$ and energy decrement $P_{bat-dis}$, which tells how much energy is charged into or discharged from the energy storage during the time interval. At the end of a time interval, this increment is added to the current energy level of the energy storage. In the next iteration, the voltage level of the energy storage is evaluated from the updated

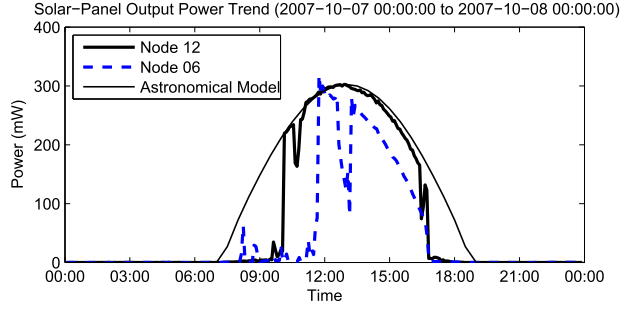


Fig. 4. Comparison of an estimation from the astronomical model with actual measurements.

energy level using the capacity-to-voltage relation of the energy storage. Note that the capacity-to-voltage relation varies over the charging rate and temperature. For a more realistic simulation, the maximum charge-discharge cycles (lifetime), self discharge rate, and temperature variations should also be considered.

4. REFINING RADIATION MODEL FOR LOCAL OBSTRUCTIONS

The estimation of solar radiation from the astronomical model can be a useful tool in understanding the long-term variation of solar radiation, but it deviates from the real measurement in many cases when the solar radiation is obstructed by objects. As shown in Figure 4, the astronomical model estimation closely matches the measurement under unobstructed view (Node 12), but it deviates further from reality upon obstruction (Node 06). In this section, we improve the accuracy of the micro-solar power system model under the effects of obstructions using the previously measured obstruction profile.

4.1 Obstructed Astronomical Model

When we estimate solar radiation under obstruction effects, we assume that objects that cause obstructions are stationary, and we can expect the same pattern of obstructions from one day to another. At time t and day n , we can define the following variables.

- $R1(t, n)$. Estimation of solar radiation using astronomical model (unit: mW).
- $M(t, n)$. Measurement of solar radiation (unit: mW).
- $Ob(t, n)$. Obstruction factor (unitless).
- $R2(t, n)$. Scaled astronomical model. $R1(t, n)$ is scaled to match the envelop of the measurement $M(t, n)$. When S is such a scaling factor, $R2(t, n)$ is given as $S \cdot R1(t, n)$ (unit: mW).
- $R3(t, n)$. Obstructed astronomical model, where the solar radiation loss due to the obstruction factor is subtracted from the scaled astronomical model. $R3(t, n)$ is given as $S \cdot R1(t, n) \cdot (1 - Ob(t, n))$ (unit: mW).

Suppose t is defined over discrete time intervals t_1 through t_m , and the measurement of solar radiation $M(t, n)$ has a maximum at interval t_{max} . Then, the scaling factor S is defined as follows.

$$S = \frac{M(t_{max}, n)}{R1(t_{max}, n)}. \quad (11)$$

Using the maximum point $M(t_{max}, n)$ for the scaling factor S may produce a misleading result, depending on the profile of the solar radiation measurement. In order

to remove the case in which the maximum point is an outlier, we used a $(100-\alpha/2)\%$ -percentile point to calculate the scaling factor.

$$S = \frac{M(t_{(100-\alpha/2)\%max}, n)}{R1(t_{(100-\alpha/2)\%max}, n)}. \quad (12)$$

This removes outliers that exist outside $(100 - \alpha/2)\%$ of the node distribution. For example,

$$S = \frac{M(t_{97.5\%max}, n)}{R1(t_{97.5\%max}, n)}$$

is a scaling factor estimate that removes 5% of outliers. One may use the same scaling factor for nodes of the same design and deployment plan. However, in a real situation, each node can have a manufacturing and deployment variation, and this can lead to a large estimation error, depending on the variation. We decided to model the scaling factor for each node to achieve more accurate estimations. M , $R1$, and $R2$ are functions of location, especially of latitude, panel inclination, and panel orientation, as described by Equation (1) in Section 3.1.1.

The obstruction factor $Ob(t, n)$ is the relative difference between the scaled astronomical model $R2(t, n)$ and the measurement $M(t, n)$.

$$Ob(t, n) = \begin{cases} \frac{R2(t, n) - M(t, n)}{R2(t, n)} & \text{if } R2(t, n) > 0, \\ 1 & \text{otherwise.} \end{cases} \quad (13)$$

Note that $R2(t, n)$ is not necessarily the same as $M(t, n)$, because the scaling factor S is calculated as the ratio of $M(t, n)$ over $R1(t, n)$ at $(100-\alpha/2)\%$ -percentile point, not simply $M(t, n)$ over $R1(t, n)$.

The obstructed astronomical model at time t and date n' , $R3(t, n')$, is given as $S \cdot R1(t, n') \cdot (1 - Ob(t, n'))$. Since we assume that obstructions are stationary, $Ob(t, n') = Ob(t, n)$. Thus,

$$R3(t, n') = S \cdot R1(t, n') \cdot (1 - Ob(t, n)). \quad (14)$$

Note that the use of a scale factor is for calibrating the solar panel. A solar panel can be modeled without a scale factor when its mathematical model is available, but this may not be true in certain cases. By using a scale factor with the astronomical model, any solar panel can be modeled empirically without explicitly requiring a mathematical model for the solar panel. In addition, the scale factor can be estimated from a one-time measurement, and it does not hurt the long-term predictability of our model.

While the example above used samples from a single day to estimate the scaling factor and the obstruction vector, estimates from multiple days can be used to reduce the error. The process of creating an obstructed astronomical model is summarized in Figure 5. Figure 6 shows the measurement $M(t, n)$ with three different solar radiation estimations: the astronomical model $R1(t, n)$, the scaled astronomical model $R2(t, n)$ and the obstructed astronomical model $R3(t, n)$. Intuitively, an ideal astronomical model should have higher power than a scaled model. However, the result from an astronomical model in Figure 6 is not calibrated yet. While it can be used to predict the trend, it should be calibrated when it is compared with the measurement. When the scaling factor is greater than one, the scaled model has higher power than the astronomical model.

In the preceding, we used a one-time measurement of solar radiation profile $M(t, n)$ as a reference obstruction profile, assuming that obstructions are mostly stationary and the effects of any moving objects are transient; however, this approach may not

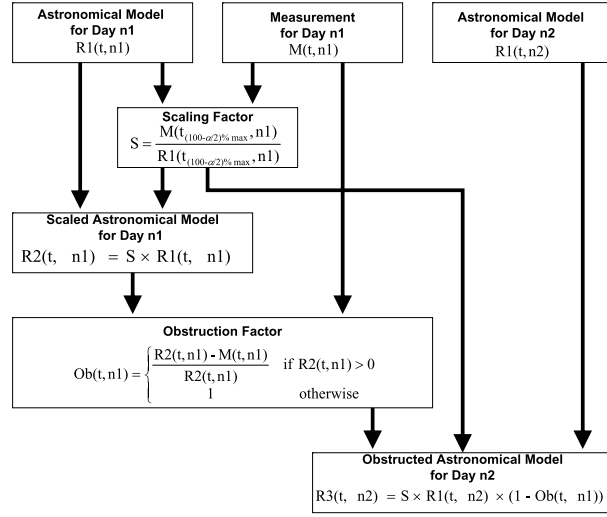


Fig. 5. Obstructed astronomical model.

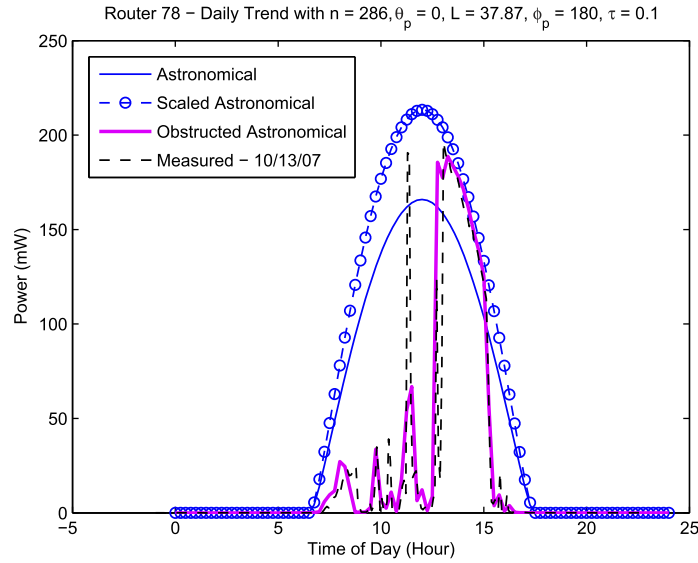


Fig. 6. Estimating the solar radiation using obstruction measurement.

capture the change when moving objects, such as vehicles, snow, ice, and water become part of the landscape. To estimate obstructions from mobile objects as well as stationary ones, we can extend the obstructed astronomical model by using the peak of the solar radiation profile in recent history, $M1(t, n, w)$, instead of the one-time measurement $M(t, n)$. $M1(t, n, w)$, the peak profile for day n over the last w days, can be defined as follows if we assume that we have one-time measurements $M(t, n')$ for $n' \in W = \{n - w, n - w + 1, n - w + 2, \dots, n - 1\}$.

$$M1(t, n, w) = \max_{n' \in W} M(t, n'). \quad (15)$$

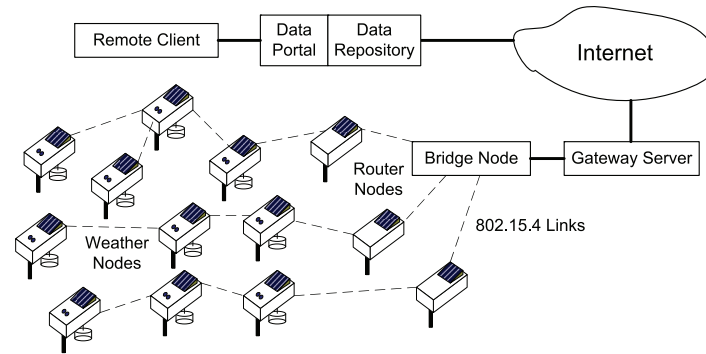


Fig. 7. System architecture for the HydroWatch micro-climate network.

4.2 Node and Network Design of Reference Implementation

In this section, we describe the reference implementation of a micro-solar power system, the HydroWatch node.

4.2.1 Network Architecture. The sensor node is built around the TelosB-compatible Tmote Sky⁸, as shown in Figure 7. The mote software, which provides periodic data acquisition, thresholding, power management, remote command processing, and health monitoring, is a modified Primer Pack/IP based on TinyOS 2.0⁹. The patch network is an implementation of IPv6 using 6LoWPAN over IEEE 802.15.4 radios [Montenegro et al. 2007]. It utilizes a packet-based form of low-power listening [Polastre et al. 2004] to minimize idle listening. Data collection is implemented as UDP packets with the routing layer using hop-by-hop retransmissions and dynamic rerouting in a redundant mesh (up to three potential parents) to provide path reliability on lossy links. It utilizes Trickle-based [Levis et al. 2004] route updates for topology maintenance. Source-based IPv6 routing is used to communicate directly to specific nodes, and dissemination is performed as a series of IPv6 link-local broadcasts. The base station is a Linux-class gateway server that provides a Web services front-end, a PostgreSQL database for information storage and retrieval, and a Web-based management console. It is also an IP router, permitting end-to-end connectivity to the patch nodes. The server facilitates such tasks as monitoring overall network health remotely, diagnosing misreporting or missing nodes, and checking the quality of links a node has to its neighbors—a function which proved critically important during the deployment phase.

4.2.2 Micro-Solar Power Subsystem of the HydroWatch Node. The core of the node design is a flexible power subsystem board that ties together a solar panel, an optional input regulator, a battery, and a switching output regulator, as shown in Figure 8. It provides measurement points for a number of electrical parameters that can be connected to the mote ADCs, sampled and recorded along with the environmental measurements. In our configuration, these monitoring features produce time-series logs of solar panel voltage, solar panel current, and battery voltage, in addition to the logs of sensor data from the application and link/neighbor data. All of these measurements are collected and stored by the gateway server, enabling deeper analysis of the performance of the node and network under varying solar conditions. The solar board also provides the mechanical structure that attaches the mote to the enclosure. The HydroWatch board

⁸Sentilla Tmote Sky. <http://www.sentilla.com/pdf/eol/tmote-sky-datasheet.pdf>.

⁹Arch Rock Corporation, Primer Pack/IP. http://www.archrock.com/downloads/datasheet/primerpack_datasheet.pdf.

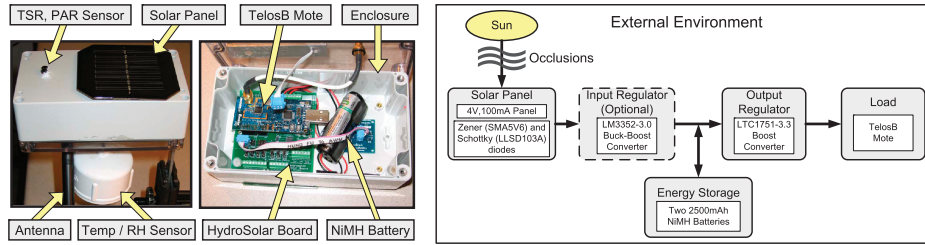


Fig. 8. HydroWatch weather node and its micro-solar power subsystem.

was designed to permit the study of a variety of power subsystem options. The solar panel and the battery are attached through screw terminals. Headers and mounting holes permit direct attachment of TelosB form factor motes, but a mote of any other type can be attached to the board through screw terminals. Additionally, the board has a prototyping area which can be used to change the power subsystem configuration. In fact, we were able to change any of the circuit elements originally used in the board schematic by simply changing jumper settings and populating the prototyping area. We used this flexibility to evaluate candidate parts for each component and quantify their contribution to the efficiency of the entire system.

This section provides the rationale and key criteria for selecting specific components, as seen through the lens of our experience designing the HydroWatch board. We begin with an analysis of application load—this directly impacts the selection of the other components in the design. The components ultimately selected for the HydroWatch micro-solar board are summarized in Table II.

Load. To get a notion of the power requirements of a node, we empirically measured the load created by our application. As is typical of sensor networks for environmental data collection, nodes alternate between a low-power state roughly 99% of the time and brief higher-power active periods. The gateway server provides estimates of the duty cycle for the MCU (0.4%) and the radio (1.2%). The peak active current is 23 mA with the MCU on and the radio in RX mode, the sleep current is around 15 μ A, and the RMS average current is 0.53 mA. We use our application load requirement to guide our selection of the rest of the components.

Energy Storage. Table III lists a number of possible rechargeable energy storage options that can be used for micro-solar power systems. We considered a number of characteristics, including capacity, operating range, energy density, and charging method. Employing the measured average consumption of our application of 0.53mA at 3.3V and the efficiency of the output regulator estimated at 50%, the daily energy requirement from the energy storage element is 79.2 mWh. This energy requirement drives the storage selection process. First, we compared each type of storage based on capacity in Table IV. All options except the supercapacitor can provide energy for more than 30 days of operation without recharging—long enough to operate for a number of days in the absence of solar radiation. For our application, even with loose physical sizing constraints, lead-acid batteries are not plausible because of low energy density. NiCd batteries have a similar footprint and charging method as NiMH batteries, but with a much smaller capacity. Additionally, NiCd chemistries are less environmentally friendly and far more susceptible to the memory effect, which can significantly reduce battery capacity over time.

Table II. Components for the HydroWatch Board

(a) Solar Panel (Silicon Solar #16530)	
V_{oc}, I_{sc}	4.23V, 111.16mA
MPP	276.0mW at 3.11V
I-V curve	$I = I_{sc} - A \cdot (\exp(B \cdot V) - 1)$ where $I_{sc} = 111.16mA$, $A = 0.2526$, $B = 1.4255$
Dimension	2.3in x 2.3in
Material, Efficiency	Polycrystalline silicon, 13%
(b) Input Regulator (LM3352-3.0: Optional)	
Manufacturer-provided efficiency	65%–83% ($I_{out} = 5mA-100mA$, $V_{out} = 3.0V$, $V_{in} = 2.5V-3V$)
Measured efficiency	54.71%–65.40% ($I_{solar} = 0mA-100mA$, $V_{out} = 3.0V$)
(c) Energy Storage	
Configuration	Two AA NiMH batteries in series
Voltage	2.4V nominal, 2.6V–3.0V at charge
Capacity	$2 \times 1.2V \times 2500mAh = 6000mWh$
(d) Output Regulator (LTC1751-3.3)	
Manufacturer-provided efficiency	55%–60% ($I_{out} = 0.1mA-20mA$, $V_{in} = 2.75V$, $V_{out} = 3.3V$)
Measured efficiency	49.69%–52.15% ($I_{out} = 3mA-6mA$, $V_{in} = 2.55V-2.71V$, $V_{out} = 3.3V$)
(e) Load	
Mote platform	Tmote Sky / TelosB mote
Vcc	2.1V–3.6V, 2.7V–3.6V with flash
Average current	App.-Dependent; 0.53mA for ours
Maximum current	23mA with MCU on, radio RX

For the decision between Lithium-based chemistries and NiMH, we drew on previous experience from the Trio deployment [Dutta et al. 2006]. Our desire to avoid having software in the charging loop (ultimately to allow nodes to simply charge when placed in the sun entirely independent of their software state), coupled with the complexity of integrating a hardware Li-ion charger, dictated the selection of NiMH, as it operates with more straightforward charging logic. This choice does present some drawbacks, however. This chemistry suffers from a self-discharge rate of 30% per month and an input-output efficiency of roughly 66%, both worse than that of any other battery chemistry considered. The practical implication of this is that for every three units of energy that are input to a battery, only two units of energy are output. We felt this cost was overcome by the simplicity of the charging logic. A two-cell configuration would enable the potential to operate without an input regulator; this choice is further discussed in this section. For increased capacity, it would be possible to put two-cell packs in parallel. Additionally, since the discharge curve of NiMH batteries is relatively flat, most of the discharge cycle produces a near-constant voltage.

Solar Panel. In selecting an appropriate panel for a micro-solar subsystem, the critical factors are the panel’s IV curve (specifically, the MPP), its cell composition, and its physical dimensions. Care should be taken in selecting a panel that will operate near its MPP given the load it is expected to support, be it a combination of an input regulator and energy storage or energy storage alone. The cell composition, that is, how many cells are present and their serial/parallel arrangement, becomes a factor

Table III. Different Types of Energy Storage Elements for Micro-Solar Power Systems

Type	Lead Acid	NiCd	NiMH
Make	Panasonic	Sanyo	Energizer
Model No.	LC-R061R3P	KR-1100AAU	NH15-2500
Characteristics of a single storage element			
Nominal voltage	6.0 V	1.2 V	1.2 V
Capacity	1300 mAh	1100 mAh	2500 mAh
Energy	7.8 Wh	1.32 Wh	3.0 Wh
Weight energy density	26 Wh/Kg	42 Wh/Kg	100 Wh/Kg
Volume energy density	67 Wh/L	102 Wh/L	282 Wh/L
Weight	300 g	24 g	30 g
Volume	116.4 cm ³	8.1 cm ³	8.3 cm ³
Self-discharge (per month)	3%–20%	10%	30%
Charge-discharge efficiency	70%–92%	70%–90%	66%
Memory effect	No	Yes	No
Charging method	trickle	trickle/pulse	trickle/pulse

Type	Li+	Li-polymer	Supercap
Make	Ultralife	Ultralife	Maxwell
Model No.	UBP053048	UBC433475	BCAP0350
Characteristics of a single storage element			
Nominal voltage	3.7 V	3.7 V	2.5 V
Capacity	740 mAh	930 mAh	350 F
Energy	2.8 Wh	3.4 Wh	0.0304 Wh
Weight energy density	165 Wh/Kg	156 Wh/Kg	5.06 Wh/Kg
Volume energy density	389 Wh/L	296 Wh/L	5.73 Wh/L
Weight	17 g	22 g	60 g
Volume	9.3 cm ³	12.8 cm ³	53.0 cm ³
Self-discharge (per month)	< 10%	< 10%	5.9%/day
Charge-discharge efficiency	99.9%	99.8%	97%–98%
Memory effect	No	No	No
Charging method	pulse	pulse	trickle

Table IV. Estimated Operating Time of a Node Without Energy Storage Recharging

Type	Lifetime
Lead Acid (LC-R061R3P)	98.5 days (= 7800mWh / 79.2mWh/day)
Two NiCd (KR-1100AAU)	33.3 days (= 2 × 1320mWh / 79.2mWh/day)
Two NiMH (NH15-2500)	75.8 days (= 2 × 3000mWh / 79.2mWh/day)
Li-ion (UBP053048)	35.4 days (= 2800mWh / 79.2mWh/day)
Li-polymer (UBC433475)	42.9 days (= 3400mWh / 79.2mWh/day)
Supercap (BCAP0350)	3.8 days (= 304mWh / 79.2mWh/day)

when the solar panel is partially occluded. Last, the physical dimensions of the panel should be compatible for the choice of enclosure. For the HydroWatch power subsystem, we selected a 4V-100mA panel from Silicon Solar Inc., whose characteristics are summarized in Table II(a) and whose IV and PV curves are illustrated in Figure 9. The MPP of this panel occurs at 3.11V, which makes it appropriate for charging 2 NiMH cells directly. Additionally, using our rule of thumb of 30 minutes of sunlight per day, the solar energy generated by this panel at its MPP is 139 mWh, satisfying the 120 mWh (= 79.2 mWh/66% NiMH charge-discharge efficiency) per day requirement of our application.

Input Regulator. In selecting the input regulator, the important parameters are the operating range of the solar panel and batteries and the method and logic used to charge the battery. In our design, we chose to trickle charge the batteries, because

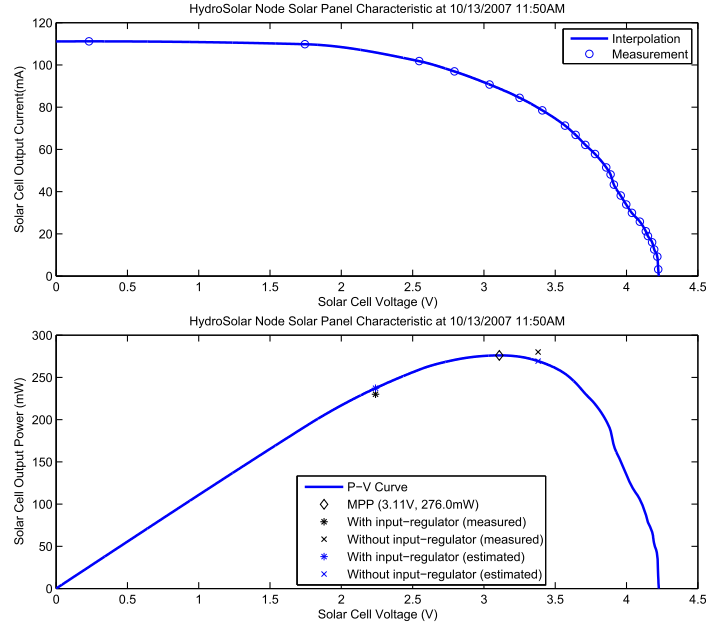


Fig. 9. Current-voltage and power-voltage performance of the Silicon Solar 4V-100mA solar panel.

it requires only a simple circuit and no software control. For trickle charging, the solar panel and the battery should be sized to meet the following condition $I_{max-solar} \leq 0.1C/hour$, where C is the nominal capacity of the battery. The HydroWatch node has a solar panel of peak current 100mA and NiMH batteries of capacity 2500mAh, and this gives $I_{max-solar} = 100mA$ and $0.1C/hour = 250mA$. Thus, the design of the HydroWatch node meets the trickle-charging condition. In our initial design of the HydroWatch board, we used an input regulator to limit the voltage to the battery. However, we observed that the existence of the input regulator forced the solar panel to operate at a point far from its MPP. Not using the input regulator results in significantly more energy harvested from the solar panel, because the input impedance of the regulator is less than that of the battery (see the bottom graph of Figure 9). In addition to this increase, energy is no longer consumed by the input regulator, which empirically has about a 60% efficiency factor. This substantial gain in total system energy as well as efficiency led us to remove the input regulator from our design; removing the input regulator is only an option, because the operating voltage of the solar panel matches the charging voltage of the batteries.

Output Regulator. The key criteria for choosing an output regulator are the operating ranges of the batteries and the load, as well as the efficiency of the regulator over the range of the load. With our choice of two NiMH AA batteries, the nominal voltage of the energy storage is 2.4V, so a boost converter is required to match the 2.7–3.6V operating range of TelosB motes (Table II(e)). The output regulator also has the important responsibility of providing a stable supply voltage to ensure the fidelity of sensor data. Though DC-DC converters introduce high-frequency noise from the switching process into the output signal, the amplitude of the noise does not negatively affect the sensor readings. If noise were a critical factor, either a low-pass filter or a higher voltage energy supply in combination with a linear drop out (LDO) regulator could be

used instead. We chose the LTC1751 regulator¹⁰, which had an efficiency of around 50%. It requires very few discrete parts and has low, constant switching noise.

4.3 Validating the Obstructed Astronomical Model

We validate the obstructed astronomical model using the deployment data of a network of HydroWatch nodes in an urban neighborhood to assess whether the model we developed accurately estimated the generation and consumption of energy in a variety of solar conditions. We deployed 22 nodes in an urban neighborhood in Berkeley; nodes were placed in varied locations, including on a house gutter, in and under trees, among shrubbery, and in a grassy yard. We measured the solar radiation profiles for these nodes from 10/7/2007 to 10/9/2007, using the measurement on 10/7/2007 as the reference for the obstruction model.

Looking at the daily graph of solar current experienced at each of the three representative nodes on a sunny day (shown in Figure 10), we can see the variations in available solar energy inputs among nodes throughout a day. Nodes that generated very little solar energy still had a solar panel voltage above three volts for the light portion of the day. This voltage is limited by the load—in this case, the batteries. Thus, the solar voltage exhibits near-binary behavior between zero volts when there is no incident light and its maximum voltage (as dictated by its load) any time between dawn and dusk.

Additionally, these current graphs are plotted alongside the three estimation models (astronomical, scaled astronomical, and obstructed astronomical), as a basis for comparison. The measurement of the solar profile fits the astronomical model when the solar panel has an unobstructed view of sunlight for a certain period of time. For other cases, whether the solar panel is obstructed during part of the day (Nodes 12 and 06) or the whole day (Node 03), the estimation from the astronomical model deviates far from the measurement. The obstructed astronomical model captures the shading effect and gives a better fitting to the measurement than the astronomical model. On an overcast day, the gap between the measurement and the estimation of each model becomes higher (as shown in Figure 11), because the estimation models capture time variation and obstruction effects, but not the weather effects. Table V summarizes the daily solar panel output measurement and estimations for both a sunny day (10/8/2007) and an overcast day (10/9/2007). We can see that the astronomical model has a higher estimation error, as the node is obstructed for longer hours; thus, the obstruction model fits the measurement on any obstruction conditions.

4.4 Long-Term Behavior and Limitation of Obstructed Astronomical Model

The obstructed astronomical model fits into the measurements well on a sunny day but does not on an overcast day. The solar radiation becomes smaller due to the weather effect, and the obstructed model does not catch this variation well with the estimation error getting higher. To study the effect, of weather variations on solar radiation and the long-term behavior of the obstructed astronomical model, we use a long-term measurement of HydroWatch weather nodes that is taken in an obstructed environment and compare the measurement data with the estimation models.

In order to see the effect of weather variations, we deployed five HydroWatch weather nodes on the rooftop of the Valley Life Science Building (VLSB) at UC Berkeley where micro-solar nodes could get solar radiation without any obstructions from trees or other buildings (see Figure 12). Since there are no obstructions between each

¹⁰Linear Technology. LTC1751: Micropower, Regulated Charge Pump DC/DC Converter. <http://www.linear.com/pc/downloadDocument.do?navId=H0,C1,C1003,C1039,C1133,P1904,D2062>.

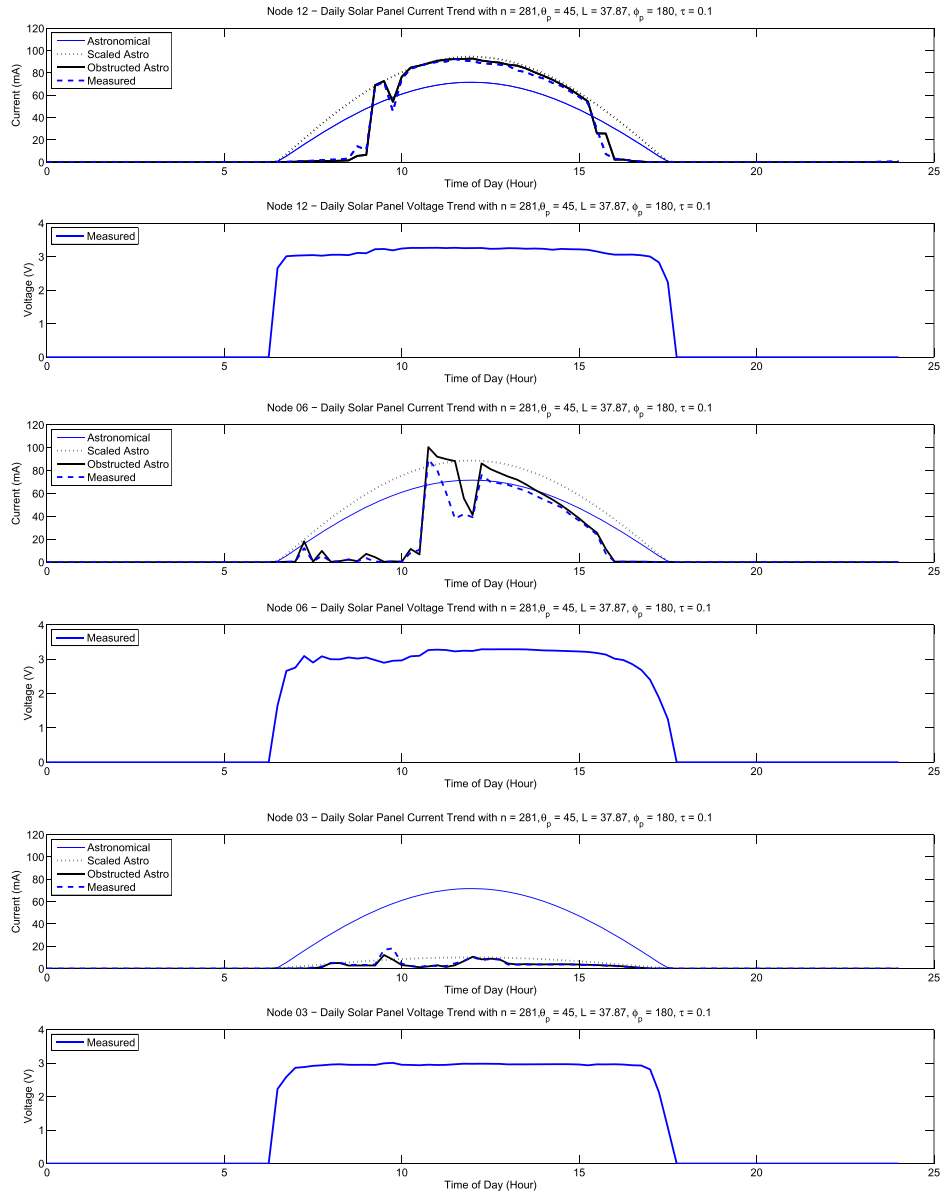


Fig. 10. Comparison of solar panel output current and voltage on a sunny day (10/8/2007) for best, worst, and middle mode in the urban neighborhood deployment. Notice the differences in the scale of the graphs.

node and the sun, the measurement of the solar panel output depends only on the diurnal and seasonal variation of solar radiation and the weather variation. The astronomical model gives an estimation of diurnal and seasonal variation of the solar radiation. We use the obstructed astronomical model in order to fit the astronomical model to the measurement, then we account for the weather effect by comparing the solar panel output measurement with the prediction from the obstructed astronomical model.

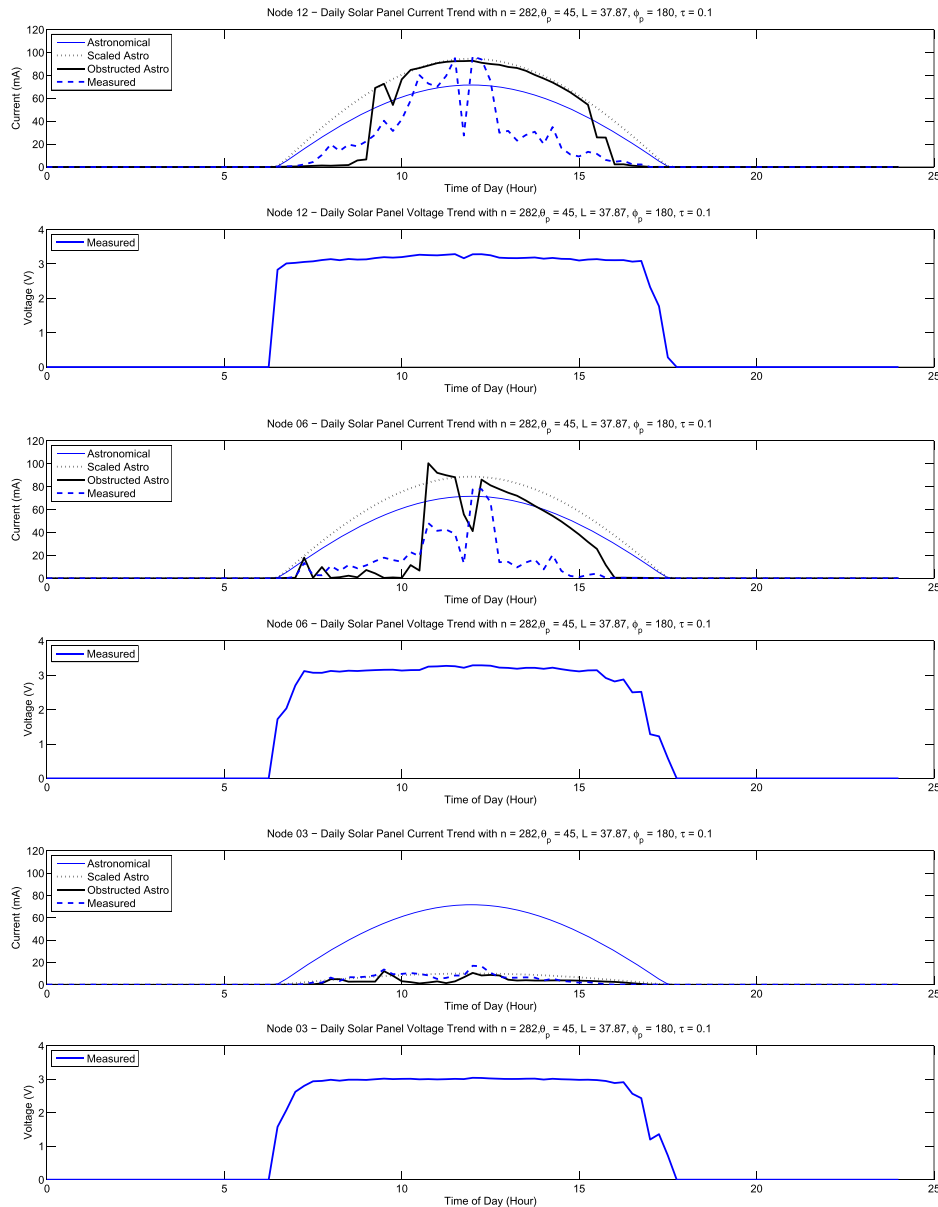


Fig. 11. Comparison of solar panel output current and voltage on an overcast day (10/9/2007) for the urban neighborhood deployment.

From Figure 13 that compares the daily solar panel energy measurement with a few estimation models, we can observe the following.

- (1) *Seasonal Variation.* The three estimation models—astronomical, scaled astronomical, and obstructed astronomical—capture the seasonal variation well, and the obstructed astronomical model tracks the peak of the measurement.

Table V. Daily Average of the Solar Panel Output Power for Different Estimation Models

(a) Node with highest solar radiation (Node 12)				
	Astronomical Model	Scaled Astro Model	Obstructed Astro Model	Measurement
On a sunny day (10/8/2007)	1691.2 mW (2.4%)	2217.6 mW (25.6%)	1721.8 mW (4.2%)	1649.7 mW
On an overcast day (10/9/2007)	1691.2 mW (38.8%)	2217.6 mW (53.4%)	1721.7 mW (39.9%)	1034.5 mW
(b) Node with median solar radiation (Node 06)				
	Astronomical Model	Scaled Astro Model	Obstructed Astro Model	Measurement
On a sunny day (10/8/2007)	1691.2 mW (44.1%)	2079.1 mW (54.5%)	1137.7 mW (16.8%)	946.1 mW
On an overcast day (10/9/2007)	1691.2 mW (66.8%)	2079.1 mW (73.0%)	1137.7 mW (50.6%)	561.9 mW
(c) Node with lowest solar radiation (Node 03)				
	Astronomical Model	Scaled Astro Model	Obstructed Astro Model	Measurement
On a sunny day (10/8/2007)	1691.2 mW (92.5%)	235.0 mW (46.0%)	127.0 mW (0.1%)	126.9 mW
On an overcast day (10/9/2007)	1691.2 mW (89.7%)	235.0 mW (26.1%)	127.1 mW (36.6%)	173.7 mW

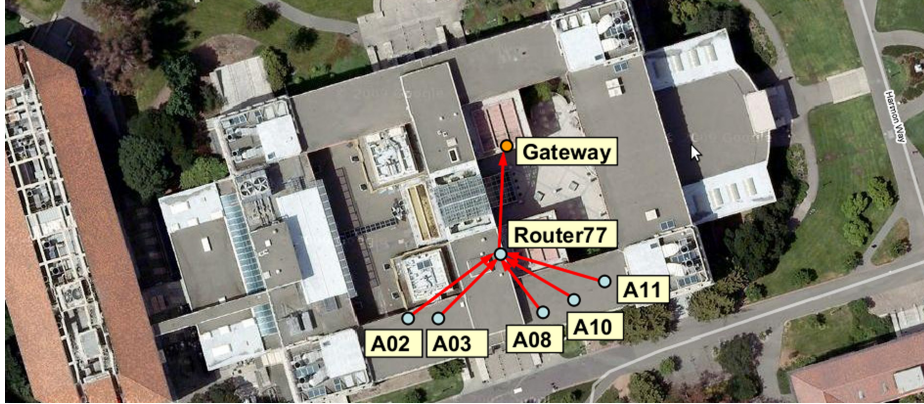


Fig. 12. Deployment map of HydroWatch nodes on the rooftop of the Valley Life Science Building at UC Berkeley. The experiment was conducted from 12/22/2007 ($n = 356$) to 4/15/2008 ($n = 365 + 106$) at Berkeley, CA (37.87°N). As for solar panel inclination θ_p and orientation ϕ_p , nodes A02 and A08 had their panels tilted 45° ($\theta_p = 45$) facing south ($\phi_p = 180$), respectively, and nodes A03, A10, and A11 had their panels flat to the ground ($\theta_p = 0$).

(2) *Weather Effect.* The obstructed astronomical model deviates from the measurement within about 30% due to weather.

In Figure 13, one may say that the astronomical model is a better estimator than the scaled astronomical model because it is closer to the measured result; however, this is not necessarily true. While the astronomical model is useful to see the trend of solar radiation, its absolute value is not meaningful because it is uncalibrated. Whereas, the scaled astronomical model is calibrated and can be used to compare against the

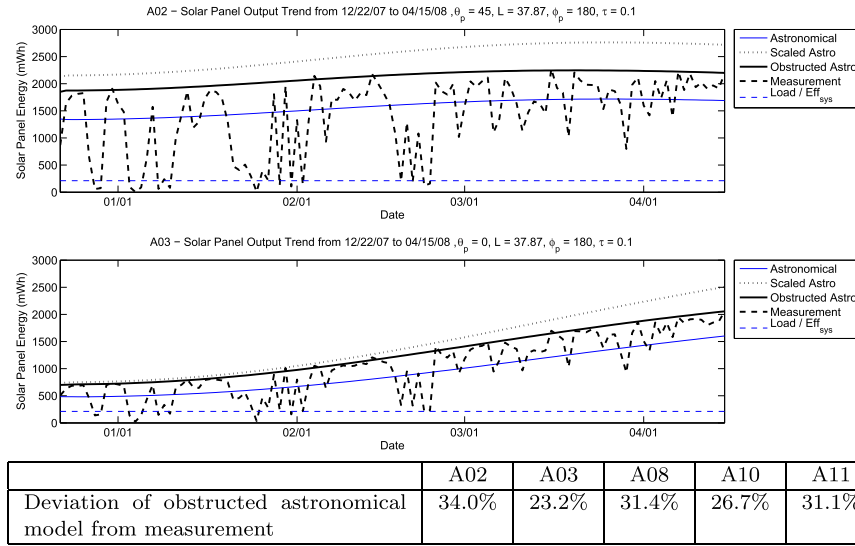


Fig. 13. Seasonal solar radiation variation of HydroWatch weather nodes on the rooftop of the Valley Life Science Building at UC Berkeley. Nodes with the same solar panel inclination had similar trends: A08 had a similar trend with A02 ($\theta_p = 45^\circ$); A10 and A11 had similar trends with A03 ($\theta_p = 0^\circ$).

measurement. It also gives the upper bound of solar radiation with no obstruction. Figure 13 actually shows the benefits of an obstructed astronomical model. The obstruction model accounts for the loss of solar radiation due to obstruction and gives a more accurate estimation than the scaled astronomical model.

5. REFINING THE RADIATION MODEL FOR WEATHER EFFECTS

5.1 Developing the Weather-Effect Model

In the previous section, we have shown that solar radiation estimation using astronomical and obstruction models has a variation of about 30% from the actual measurement due to weather effects. To predict solar radiation under weather variations, we develop a weather-effect model using publicly available data (e.g., *atmospheric turbidity*, *horizontal visibility*, and *cloud cover*) and evaluate whether the model can predict the variation of solar radiation with sufficient accuracy.

5.1.1 Atmospheric Turbidity. Atmospheric turbidity, or simply turbidity, is used as a measure of air pollution in the atmospheric science community and is known to be highly correlated with solar radiation [Cannon and Hulstrom 1988; Peterson et al. 1978; Robinson and Valente 1982]. As sunlight traverses the atmosphere, solar irradiance is degraded by several causes: sunlight can be scattered by air molecules (Rayleigh scattering); it can be absorbed by atmospheric gases, such as ozone, water vapor, and carbon dioxide; or it can be absorbed by aerosols, such as clouds, fog, and smog. Turbidity accounts for the degradation of solar radiation due to aerosols, and it is defined as the ratio of solar irradiance degraded by aerosols to extraterrestrial solar irradiance, which can be estimated using an astronomical model of solar radiation. Since solar irradiance and Rayleigh scattering varies depending on wavelength of sunlight, turbidity is typically defined at a particular wavelength. Turbidity at wavelength λ , $B(\lambda)$ is a nonnegative number and is logarithmically related to the ratio of

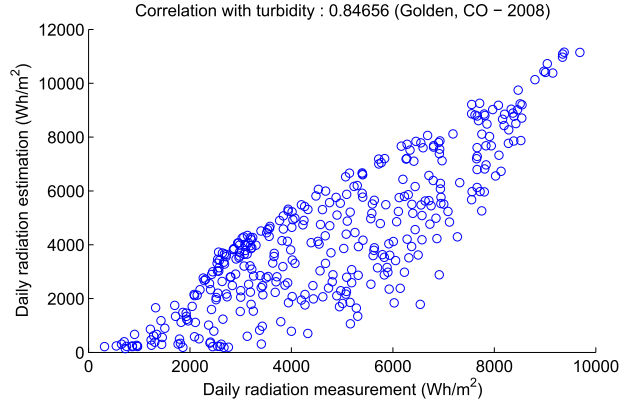


Fig. 14. Correlation of daily solar radiation estimation using turbidity and actual measurements at Golden, CO, from 1/1/2008 to 12/31/2008.

actual solar irradiance $J(\lambda)$ to extraterrestrial solar irradiance $J_0(\lambda)$ [Robinson and Valente 1982].

$$J(\lambda)/J_0(\lambda) = 10^{-(R(\lambda)+Z(\lambda)+B(\lambda))m}, \quad (16)$$

where R is the Rayleigh scattering coefficient, Z is the gaseous absorption coefficient, and m is the optical air mass, which is the relative length of sunlight through the atmosphere compared to the length when sunlight is normal to the Earth's surface. While turbidity is defined at a particular wavelength, we consider modeling solar radiation under weather variation using turbidity at 500nm, which has the highest intensity across the solar radiation spectrum. Suppose turbidity and the solar radiation estimate from the astronomical model are given as $B(n, t)$ and $AST(n, t)$ on day n and time t , we can estimate the daily solar radiation under the influence of turbidity, $RB(n, t)$, using the logarithmic relation of solar radiation and turbidity.

$$RB(n) = \int_{0h}^{24h} RB(n, t) dt = \int_{0h}^{24h} k \cdot AST(n, t) \cdot e^{-B(n,t)} dt, \quad (17)$$

where k is a constant.

In order to validate this turbidity-to-radiation model, we compare the correlation coefficient between the solar radiation under the influence of turbidity and the solar radiation measurement using a publicly available database provided by the Measurement and Instrumentation Data Center (MIDC) [BMS 2008]. The MIDC database provides data for solar radiation measurement, turbidity, and astronomical estimation of solar radiation at a per-minute or per-hour scale. From this raw data, we can calculate actual solar radiation and the estimation over an n -day time window and use them to validate the turbidity-to-radiation model. Figure 14 shows the correlation trend between the daily solar radiation estimation using turbidity and actual measurements at Golden, CO, from 1/1/2008 to 12/31/2008 with a correlation coefficient of 0.847. We can see that turbidity and solar radiation has a strong correlation. The turbidity-to-radiation model can be further refined by covering solar radiation of k days, instead of a single day. Figure 15 shows the correlation trend between solar radiation using turbidity and actual measurements at Golden, CO, from 2002 to 2008 when the comparison window size is changed from a single day to 7, 15, and 30 days. We can see that the correlation gets higher as the window size gets larger, and the correlation coefficient becomes greater than 90% when the window size is set to 15 days.

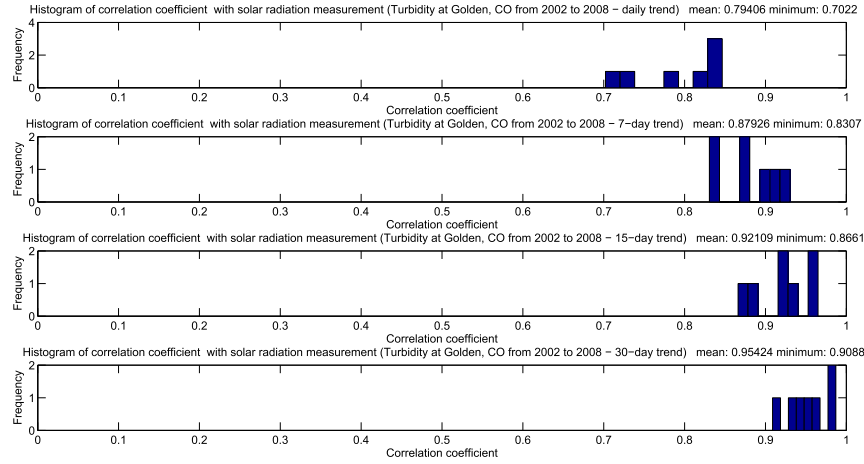


Fig. 15. Histogram of correlation of turbidity and solar radiation with different window sizes at Golden, CO, from 2002 to 2008.

While turbidity is a good estimator of solar radiation, the availability of fine-grained turbidity measurement is very limited. Thus, there is a need to develop a weather-effect model using more widely available data. Possible candidates are horizontal visibility and cloud conditions, which are available from measurement data at most airports and other weather stations.

5.1.2 Horizontal Visibility and Cloud Condition. Horizontal visibility, which is monitored at most airports to ensure air traffic safety, is the distance one can see horizontally with a maximum of 10.0 miles or 16.1 km. With horizontal visibility and a solar radiation estimate from the astronomical model being given, we can estimate daily solar radiation under the influence of the visibility using the observations of Peterson et al. on the relationship between horizontal visibility and the ultra-violet (UV) spectrum of solar irradiance [Peterson et al. 1978]. Peterson et al. stated that visibility and UV irradiance had a strong correlation below 10 km of visibility, while UV irradiance was only slightly correlated with a visibility of 12 km or above. While their observation was about visibility and UV irradiance, we apply it to develop a weather-effect model that would estimate solar radiation (not just UV spectrum) from horizontal visibility.

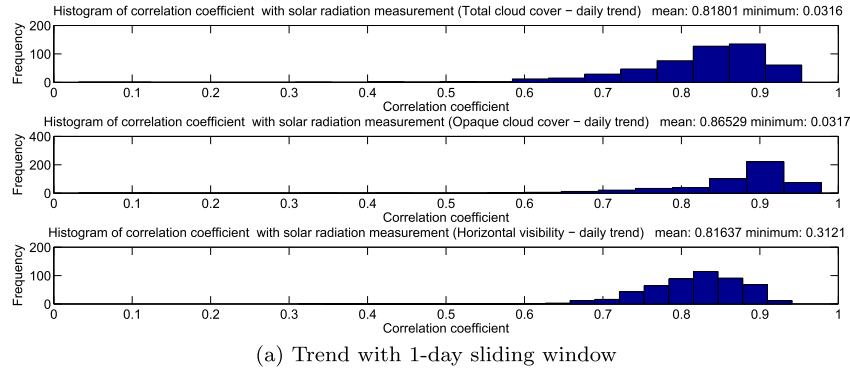
When the horizontal visibility and solar radiation estimate from the astronomical model are given as $V(n, t)$ and $AST(n, t)$ on day n and time t , we can estimate the daily solar radiation under the influence of visibility $RV(n)$ as follows.

$$RV(n) = \int_{0h}^{24h} \frac{\widehat{V}(n, t)}{V_{knee}} \cdot AST(n, t) dt ; \quad (18)$$

$$\widehat{V}(n, t) = \begin{cases} V_{knee} & V(n, t) \geq V_{knee} \\ V(n, t) & \text{otherwise} \end{cases} , \quad (19)$$

where we set V_{knee} as 12.0 km.

Cloud condition is the percentage of the sky covered by clouds, and it is used to determine the cloudiness of the sky at a particular location. Depending on whether we count all visible clouds or only opaque clouds, cloud condition can be further divided into *total cloud cover* and *opaque cloud cover*. For a given cloud condition $W(n, t)$ and solar radiation estimate from the astronomical model $AST(n, t)$ on day n and time t , we



		1 day	7 day	15 day	30 day
Total cloud cover	mean	0.81801	0.83432	0.91748	0.87498
	(minimum)	(0.0316)	(0.1147)	(0.1098)	(0.087)
Opaque cloud cover	mean	0.86529	0.87858	0.94542	0.91282
	(minimum)	(0.0317)	(0.118)	(0.1099)	(0.0871)
Horizontal visibility	mean	0.81637	0.91562	0.97454	0.93579
	(minimum)	(0.3121)	(0.5701)	(0.8448)	(0.6591)

(b) Correlation statistics for windows of 1, 7, 15 and 30 days

Fig. 16. Correlation of solar radiation measurement with solar radiation estimation using visibility and cloud condition.

can estimate $RW(n)$, the daily solar radiation under the influence of cloud condition on day n , as follows.

$$RW(n) = \int_{0h}^{24h} W(n, t) \cdot AST(n, t) dt. \quad (20)$$

In order to validate weather-effect models with horizontal visibility and cloud condition, we compare the solar radiation estimate using weather-effect models and the actual solar radiation measurements from 35 sites during 1991 to 2005, using historical measurements from the National Solar Radiation Data Base [NSR 2008].

Figure 16 shows the correlation of solar radiation measurement and estimate when we use visibility, total cloud cover, and opaque cloud cover, with the sliding window size as 1, 7, 15, and 30 days. For the weather-effect models using horizontal visibility, total cloud cover, and opaque cloud cover, we can observe the following. First, the weather-effect models show high correlation with the actual measurements when the estimation is based on a sufficient number of samples. For example, weather-effect models with total cloud cover, opaque cloud cover, and horizontal visibility have mean correlations of 89%, 93%, and 96%, respectively, for a window size of 15 days. Second, the estimation quality of the weather-effect models improves as we increase the window size, but it reaches a sweet spot at 15 days. When we increased the window size from 15 days to 30 days, the improvement in the correlation coefficient was marginal. Third, horizontal visibility is a better predictor of solar radiation than total cloud cover or opaque cloud cover. The mean and the minimum of the correlation coefficient of horizontal visibility are 96% and 79%, respectively, with a 15-day window. Whereas, total cloud cover and opaque cloud cover have much wider distributions. While the mean of their correlation coefficients is about 90%, the minimum of the correlation coefficients is much smaller, making long tails (9% and 10%).

5.2 Evaluating the Weather-Effect Model

In the previous section, we have shown that horizontal visibility and cloud condition can be used to estimate the solar radiation under the weather effect due to their relatively high correlation with solar radiation and wide availability from many weather stations. In this section, we validate this idea with a concrete example. We will develop a solar radiation weather-effect model using the historical data of horizontal visibility and cloud conditions from a publicly available weather station and compare it with the five-month long solar radiation measurements from our reference implementation of a micro-solar power system.

5.2.1 Defining Solar Radiation Estimators. In order to develop a weather-effect component, we use data from a publicly available online weather station, Wunderground.¹¹ Wunderground provides a live and archived view of several weather metrics for a number of weather stations across the United States. We have used archived data of horizontal visibility and cloud conditions for the Oakland International Airport, which is the nearest weather station to the measurement site at UC Berkeley that provides fine-grained data of horizontal visibility and cloud conditions.

Suppose the solar radiation estimation without weather effect is given as $AST(t)$, and the weather factor $W(t)$ can be represented as a number between 0 and 1. Then, the solar radiation with weather effect $RW(t)$ can be represented as a product of $AST(t)$ and $W(t)$: $RW(t) = W(t) \cdot AST(t)$. Wunderground provides hourly weather data reports, including horizontal visibility and cloud conditions. Horizontal visibility is reported as number of miles between 0 and 10 (or 0 to 16.1 km). The cloud condition is reported in five different grades depending on the percentage of sky being covered: *clear* (0), *partly cloudy* (1/8–2/8), *scattered clouds* (3/8–4/8), *mostly cloudy* (5/8–7/8), and *overcast or fog* (1). To estimate solar radiation under weather effect, we need to translate a weather metric into the weather factor $W(t)$. The simplest way is to translate these metrics in a linear scale.

The weather factor for cloud conditions can be defined using the percentage of sky covered by clouds.

$$W(t) = \begin{cases} 1 & (= 1 - 0) & \text{clear,} \\ 0.8125 & (= 1 - 3/16) & \text{partly cloudy,} \\ 0.5625 & (= 1 - 7/16) & \text{scatter clouds,} \\ 0.25 & (= 1 - 3/4) & \text{mostly cloudy,} \\ 0 & (= 1 - 1) & \text{overcast or fog.} \end{cases} \quad (21)$$

The weather factor for horizontal visibility $Vis(t)$ can be defined as follows using the observation by Peterson et al. [1978] that solar radiation is highly correlated with visibility for visibility of less than or equal to a threshold of 12km ($= Vis_{knee}$).

$$W(t) = \begin{cases} 1 & Vis(t) \leq Vis_{knee}, \\ Vis(t)/Vis_{knee} & \text{otherwise.} \end{cases} \quad (22)$$

Figures 17(a) and 17(b) show a correlation between the estimation and measurement of solar radiation when we use horizontal visibility and cloud conditions with linear scale mapping. In both cases, correlations are not very high, with correlation coefficients being less than 0.5. This implies that estimating solar radiation with linear scale mapping is not very meaningful.

¹¹Weather Underground. <http://www.wunderground.com>.

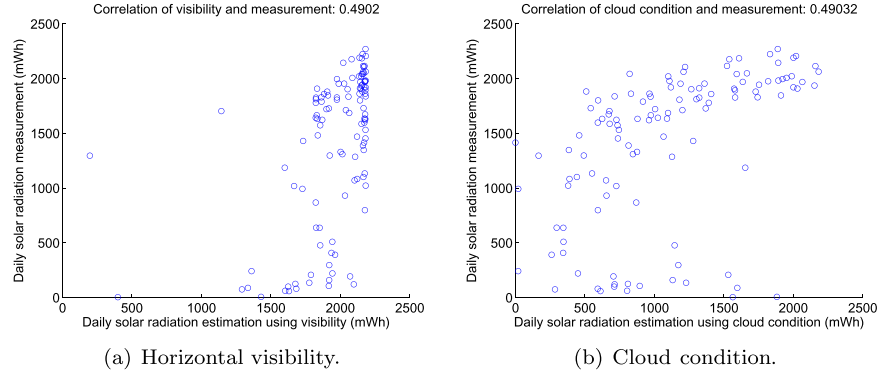


Fig. 17. Correlation of horizontal visibility and cloud conditions to the weather variation of the solar radiation using a linear scale mapping (Node A02 from 12/22/2007 to 04/15/2008).

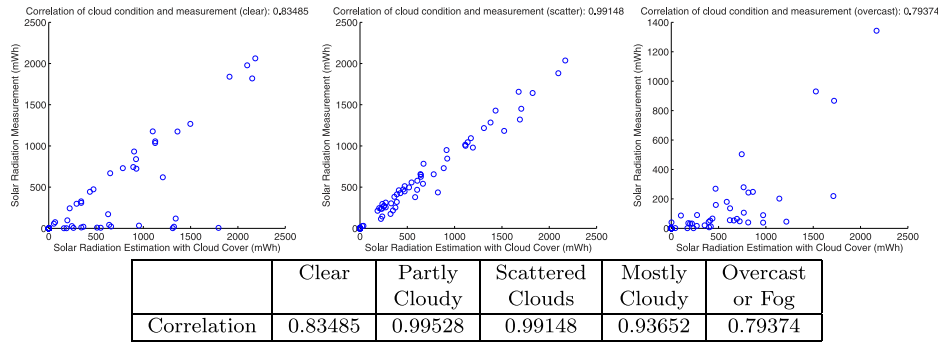


Fig. 18. Correlation trends for each disjoint set of cloud conditions.

However, these weather metrics show different trends if they are divided into smaller subgroups. Figure 18 shows a correlation between the solar radiation estimation and measurement when the cloud condition is divided into five different subgroups. We can see that there is a high correlation between the solar radiation estimation and measurement with a correlation coefficient of each subgroup between 0.79 and 0.99. Figure 19 shows a correlation between the solar radiation estimation and measurement when horizontal visibility is divided into 11 different groups: $W_1 = [0, 1)$, $W_2 = [1, 2)$, $W_3 = [2, 3)$, \dots , $W_{10} = [9, 10)$, $W_{11} = \{10\}$. We can see that with horizontal visibility, the correlation between the solar radiation estimation and measurement is low, except for the group with the highest visibility, W_{11} , which has a correlation coefficient of 0.7. While horizontal visibility has a low correlation for groups with lower visibility, the histogram in Figure 20 shows that groups with low correlation is insignificant in terms of occurrences.

5.2.2 Calibrating Solar Radiation Estimators. We have shown that we can achieve a relatively high correlation between the solar radiation estimation and measurement by dividing a weather metric into multiple subgroups. Since a weather metric has a different correlation coefficient depending on which subgroup it belongs to, the weather factor also needs to be defined for each subgroup.

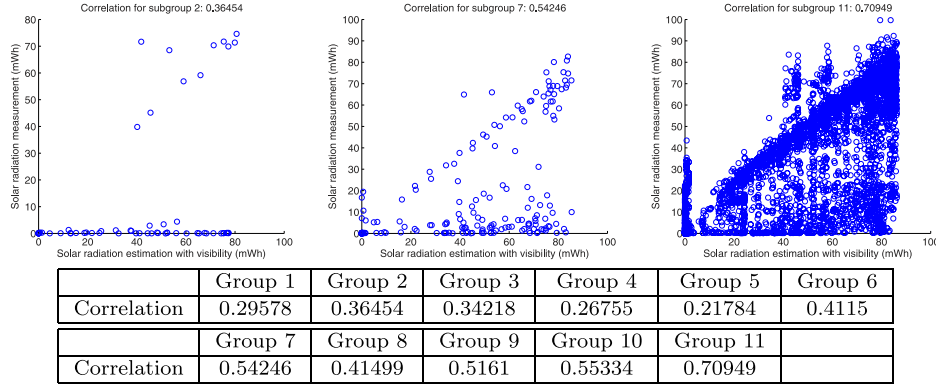


Fig. 19. Correlation trends for each disjoint set of visibility.

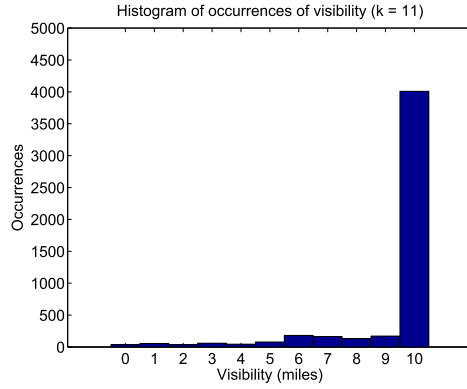


Fig. 20. Occurrences (frequency) of each disjoint set of visibility.

The weather factor $W(t)$ can be calibrated using the probability distribution of the ratio between measurements and estimations for sample points of each subgroup. Suppose the following.

- The values of weather metrics can be partitioned into k -disjoint subsets W_1, W_2, \dots, W_k .
- r_i , the ratio of the solar radiation measurements over solar radiation estimations using an obstructed astronomical model for subset W_i on day n , is given by

$$r_i(n) = \frac{Y_i(n)}{X_i(n)} = \frac{\int_{W(t) \in W_i} M(n, t) dt}{\int_{W(t) \in W_i} AST(n, t) dt}. \quad (23)$$

- r_i 's belong to $[0, r_{max}]$, and the set of r_i 's, $\{r_i\}$, is divided into $(m + 1)$ equally-spaced bins $B_0, B_1, \dots, B_j, \dots, B_m$, where

$$B_j = \left\{ \frac{Y_i}{X_i} \mid \frac{j}{m} \cdot r_{max} \leq \frac{Y_i}{X_i} < \frac{j+1}{m} \cdot r_{max} \right\} \quad \text{for } j = 0, \dots, (m-1);$$

$$B_m = \left\{ \frac{Y_i}{X_i} \mid \frac{Y_i}{X_i} \geq r_{max} \right\} \quad \text{for } j = m. \quad (24)$$

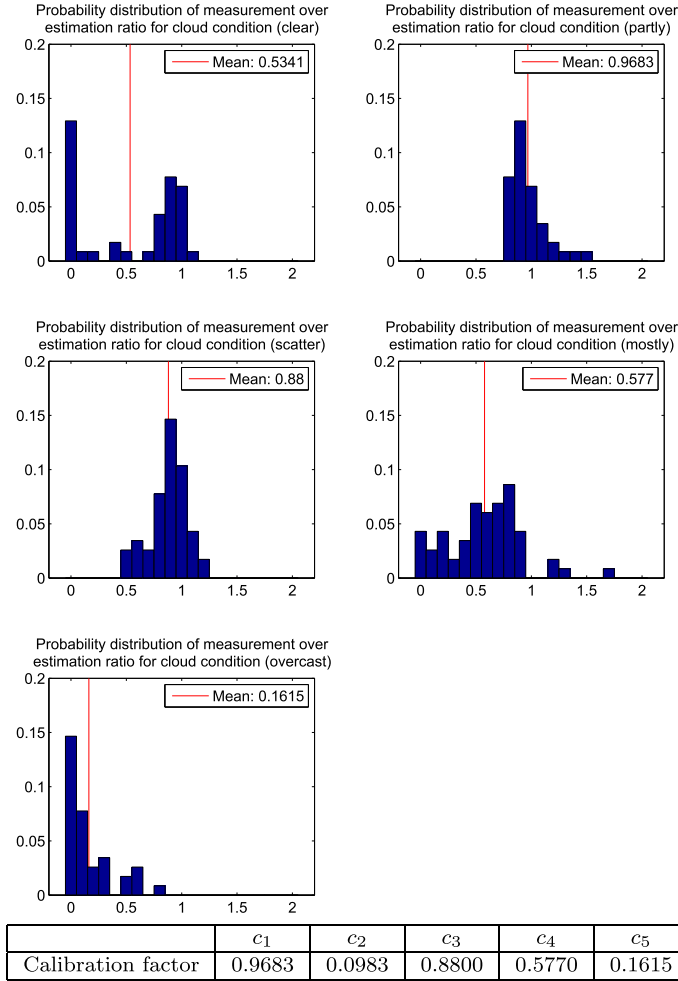


Fig. 21. Probability distribution of calibration factor for each disjoint set of cloud conditions.

Then, the probability that the ratio r_i belongs to a bin B_j is

$$P(r_i \in B_j) = |B_j|/|B_{all}|, \quad (25)$$

where B_{all} is a union of B_0 through B_m . As a calibration factor, we use the expectation of r_i , $E(r_i)$ for each subset W_i .

We can describe this process in a more concrete way for cloud conditions and visibility. For cloud conditions, the k -disjoint subsets can be defined as follows: $W_1 = \{\text{clear}\}$, $W_2 = \{\text{partly cloudy}\}$, $W_3 = \{\text{scatter clouds}\}$, $W_4 = \{\text{mostly cloudy}\}$, $W_5 = \{\text{overcast}\}$. A set of (X_i, Y_i) pairs for subset i are the (x, y) coordinates in the i th scatter plot of Figure 18. If we partition a set $\left\{\frac{Y_i}{X_i}\right\}$ into 21 bins over domain $[0, 2]$, then we can get a probability distribution, as shown in Figure 21. Figure 21 also shows the mean value of $\frac{Y_i}{X_i}$ for each subset. The overall trend is that the calibration factor becomes smaller as weather becomes more overcast. One exception is the calibration factor for the clear condition. The calculation from the sample points gives a calibration factor of 0.5341. Since we expect calibration factors to be monotonically decreasing as cloud conditions

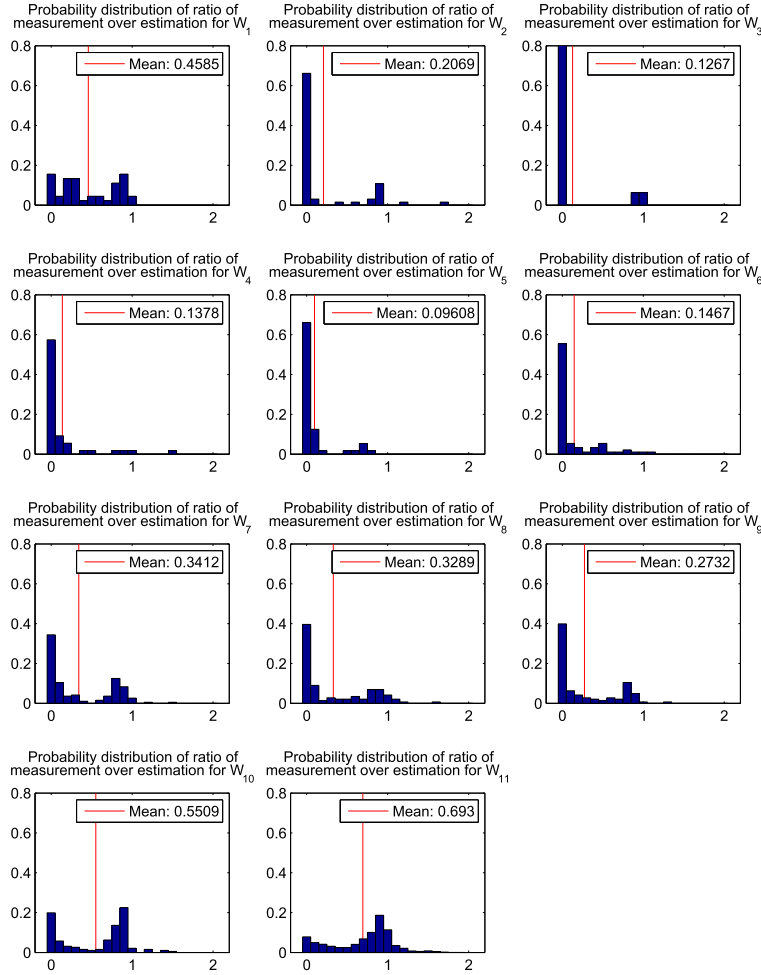


Fig. 22. Probability distribution of calibration factor for each disjoint set of visibility.

become more overcast, we set the calibration factor for the clear condition as 0.9683, which is the calibration factor for the partly cloudy condition.

For horizontal visibility, which is a real number between 0 and 10, k -disjoint subsets can be defined by partitioning the domain as follows: $W_1 = [0, \frac{10}{k-1})$, $W_2 = [\frac{10}{k-1}, \frac{20}{k-1})$, $W_3 = [\frac{20}{k-1}, \frac{30}{k-1})$, \dots , $W_{k-1} = [\frac{10 \cdot (k-2)}{k-1}, \frac{10 \cdot (k-1)}{k-1})$, $W_k = \{10\}$.

If we consider possible values for $k = 11$, k -disjoint sets can be given as follows: $[0, 1)$, $[1, 2)$, $[2, 3)$, \dots , $[9, 10)$, $\{10\}$.

A set of (X_i, Y_i) pairs for subset i are plotted in i th scatter plot of Figure 19. If we partition a set of $\{\frac{Y_i}{X_i}\}$ into 21 bins over domain $[0, 2]$, then we can get a probability distribution, as shown in Figure 22. As a calibration factor for each subset W_i , we can use the expectation of $\frac{Y_i}{X_i}$, which is shown as a vertical line in each subplot. Since horizontal visibility is given as a real number between 0 and 10 rather than a discrete set of numbers, the calibration factor should be a continuous calibration function. The desirable properties for a calibration function are to minimize the difference between the

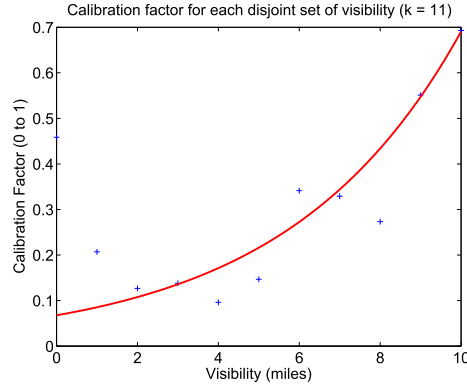


Fig. 23. An exponential curve that fits the calibration factors with minimum errors.

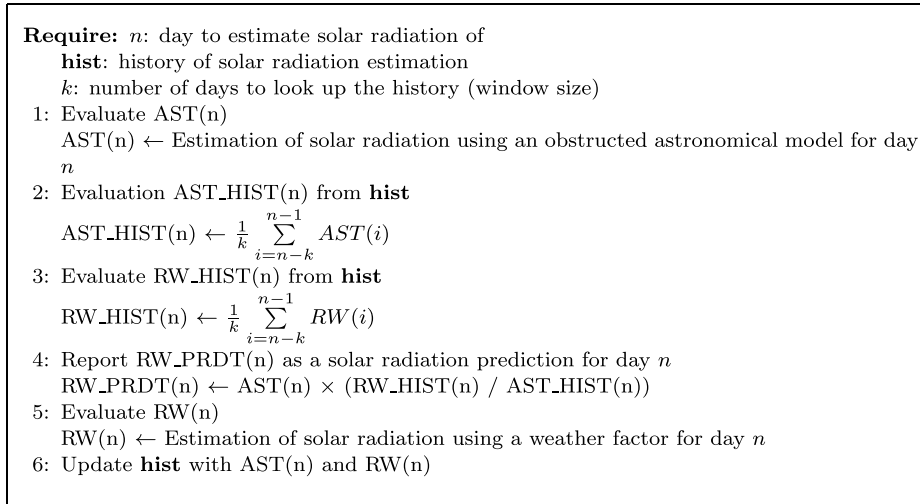


Fig. 24. Algorithm for predicting solar radiation with k -day history of weather effects.

measurements and the estimations of solar radiation and to monotonically increase as horizontal visibility increases. We have considered an exponential curve and a polynomial curve as a possible calibration function, and curve fitting with measurements and estimations of solar radiation at the Valley Life Science Building deployment has shown that an exponential curve is the best candidate. The exponential calibration function that converts a given horizontal visibility x to a number $y \in [0, 1]$ is given as follows.

$$y = a \cdot \exp(b \cdot x) \quad a : 0.06759 \text{ and } b : 0.2324. \quad (26)$$

Figure 23 shows this exponential calibration function.

5.2.3 Predicting Solar Radiation Using the History of a Weather-Effect Component. We have shown how to estimate solar radiation using a weather metric and how to calibrate such a solar radiation estimator when a sample of measurements are given for solar radiation and the weather metrics. However, these measurements of solar radiation

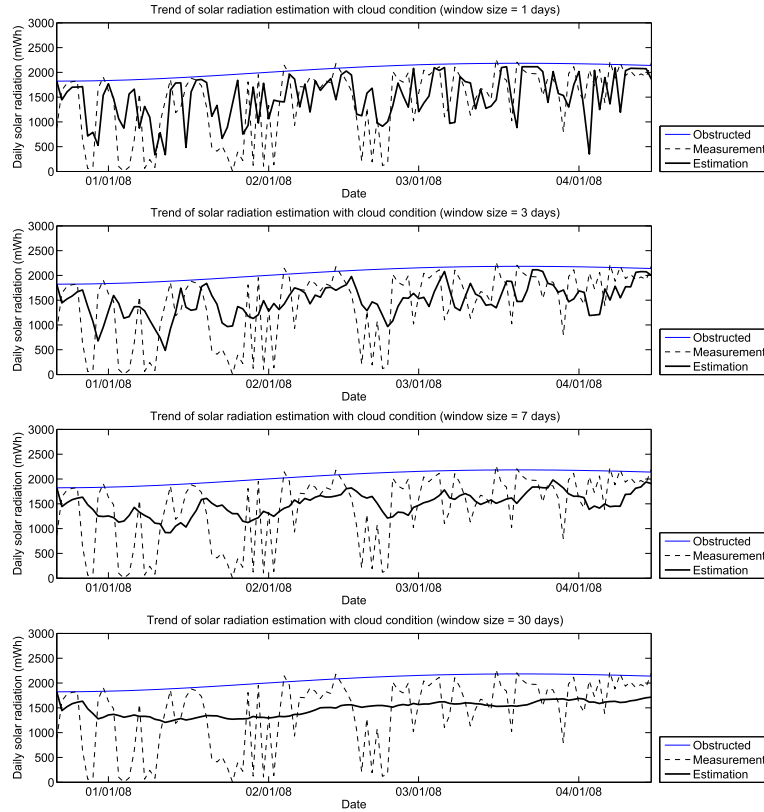


Fig. 25. Solar radiation prediction with the cloud-based model with different window sizes (node A02 in the VLSB deployment from 12/22/2007 to 04/15/2008).

and weather metrics are given only for the past and the present. In order to predict solar radiation under a weather effect for the future, we need a different model.

One possible model is to predict solar radiation using a recent history of weather metrics. Figure 24 shows an algorithm that estimates the solar radiation for day n using the astronomical model and the recent k -day history of weather metrics. As a weather factor for day n , this algorithm uses the ratio of $RW_HIST(n)$ to $AST_HIST(n)$, that is, the recent k -day average of the solar radiation estimation using the weather effect to the solar radiation estimation using an obstructed astronomical model. At the end of each iteration, the algorithm calculates $RW(n)$, which is the solar radiation estimation using a weather effect for day n , and updates the history file with $RW(n)$ so that a later iteration can look it up as history.

We estimated solar radiation using the cloud-based model and the visibility-based model for the nodes in the VLSB deployment. Figures 25 and 26 show the trend of solar radiation prediction with the models with different window sizes (1, 3, 7, and 30 days). Figure 27 shows the trend of the deviation between the prediction and the measurement as we increase the window size. We can see that the deviation is relatively high with a window size of one day, but it stabilizes after three days and converges after seven days.

Table VI shows the deviation of the prediction from the measurement when we use a window size of three and seven days. We can see that with the cloud-based model, we can estimate the trend of solar radiation within 6% of the measured value, whereas

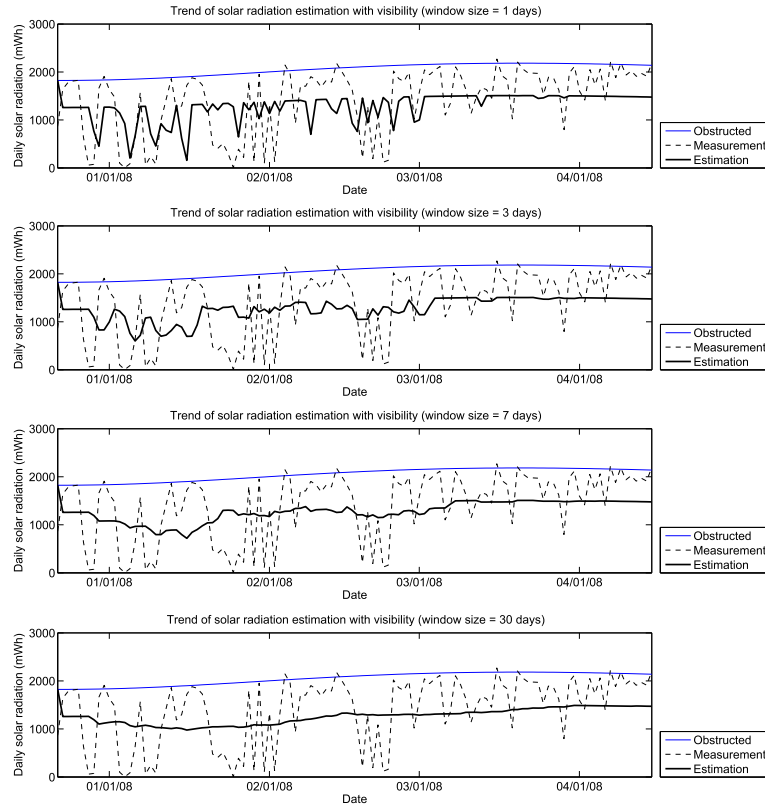


Fig. 26. Solar radiation prediction with the visibility-based model with different window sizes (node A02 in the VLSB deployment from 12/22/2007 to 04/15/2008).

not using a weather model yields an approximate 26% estimation error. We can also see that with the visibility-based mode, the estimation error is about 20%, and the predictability is not as high as that of the cloud-based model.

5.3 Summary

In this section, we have developed and evaluated a weather-metric-based model using cloud conditions and horizontal visibility, which are commonly measured in a number of weather stations and widely available. With the condition of a weather metric given, our weather metric model adjusts the solar radiation estimation of an obstructed astronomical model using the probability distribution of the weather metric, which is built with samples of the solar radiation measurement and weather metric. With the weather-metric model, we predicted the solar radiation by using a k -day history of the weather metric. With a cloud-based model, we were able to predict the solar radiation with a 6% margin of error, while maintaining three or seven days of history of the weather metric, while the prediction error is about 26% without a weather metric. With a visibility-based model, the prediction error was around 20%. One limitation of this weather-metric-based model is that the prediction is for the average behavior over a certain window of time, not for the behavior at a specific time, because our weather-metric model is a probabilistic model, and the exact pattern of the weather metric for the future is not known.

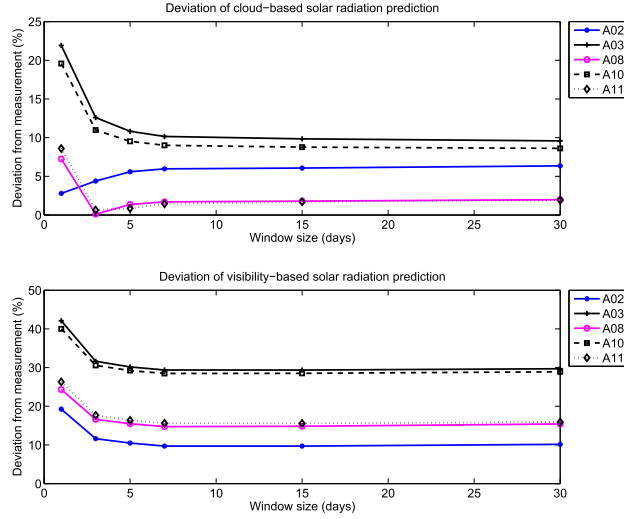


Fig. 27. Deviation of solar radiation prediction with cloud-based and visibility-based models.

Table VI. Deviation for Different Nodes

(a) With a three-day window

Models	A02	A03	A08	A10	A11	Mean	Median
Obstructed	32.02%	20.25%	28.68%	20.66%	28.67%	26.06%	28.67%
Cloud	4.39%	12.59%	0.11%	10.98%	0.63%	5.74%	4.39%
Visibility	11.61%	31.63%	16.60%	30.56%	17.67%	21.61%	17.67%

(b) With a seven-day window

Models	A02	A03	A08	A10	A11	Mean	Median
Obstructed	32.02%	20.25%	28.68%	20.66%	28.67%	26.06%	28.67%
Cloud	5.97%	10.15%	1.69%	9.01%	1.44%	5.65%	5.97%
Visibility	9.69%	31.63%	14.73%	28.47%	15.61%	19.57%	15.61%

6. CONCLUDING REMARKS

In this article, we presented a model of a micro-solar power system with realistic solar radiation models. We summarize this article as follows. First, we developed a general model of micro-solar power systems. While the design space of micro-solar power systems is very large, it is essential we use the same simulation framework to represent such diversity in a scalable fashion. We presented a general model of micro-solar power systems that consisted of several lumped elements, such as the external environment, a solar collector, an input regulator, energy storage, output regulator and a load, and their relationship in terms of energy flow and efficiency factors. Second, we developed two refinements of an astronomical model for accurately estimating solar radiation in a realistic environment: an obstructed astronomical model and a weather-metric model. The astronomical model estimates solar radiation using well-known formulas without any knowledge of the deployment site and works well on a clear day, but its estimation error can be high on an overcast day. The obstructed astronomical model refines the estimates of the astronomical model by using a few samples of local measurements, incurring a modest estimation error. The weather-metric model further refines the obstructed astronomical model by adjusting the solar radiation by the amount of weather effects. Third, we validated the two radiation models by comparing solar

energy estimates with empirical results in a realistic environment. The short-term deployment, where reference platform nodes were placed under varying solar profiles in urban neighborhoods, showed that our models could estimate the solar energy budget with only a small degree of error. The long-term deployment, where reference platform nodes were placed on an urban rooftop environment, showed that our simulation tools could estimate the solar energy budget of a system under varying weather conditions and that the difference between estimates and empirical results was bounded by roughly 30%. We reduced this estimation error even further with a weather-metric model, predicting the solar radiation with a 6% margin of error by maintaining a week of cloud condition history.

REFERENCES

- BMS. 2008. Solar Radiation Research Laboratory. http://www.nrel.gov/midc/sr11_bms/.
- CANNON, T. W. AND HULSTROM, R. L. 1988. The atmospheric optical calibration system. In *Proceedings of the 20th IEEE Photovoltaic Specialists Conference*.
- CHEN, B., JAMIESON, K., BALAKRISHNAN, H., AND MORRIS, R. 2001. Span: An energy-efficient coordination algorithm for topology maintenance in ad hoc wireless networks. In *Proceedings of the 7th Annual International Conference on Mobile Computing and Networking*.
- CORKE, P., VALENCIA, P., SIKKA, P., WARK, T., AND OVERS, L. 2007. Long-duration solar-powered wireless sensor networks. In *Proceedings of the 4th IEEE Workshop on Embedded Networked Sensors*.
- DAVE, J. V., HALPERN, P., AND MYERS, H. J. 1975. Computation of incident solar energy. *IBM J. Res. Develop.* 19, 6, 539–549.
- DUST NETWORKS. 2006. Technical Overview of Time Synchronized Mesh Protocol (TSMP). http://www.dustnetworks.com/docs/TSMP_Whitepaper.pdf.
- DUTTA, P., HUI, J., JEONG, J., KIM, S., SHARP, C., TANEJA, J., TOLLE, G., WHITEHOUSE, K., AND CULLER, D. 2006. Trio: Enabling sustainable and scalable outdoor wireless sensor network deployments. In *Proceedings of the 5th International Conference on Information Processing in Sensor Networks*.
- HANDZISKI, V., KÖPKE, A., WILLIG, A., AND WOLISZ, A. 2006. Twist: A scalable and reconfigurable testbed for wireless indoor experiments with sensor networks. In *Proceedings of the 2nd International Workshop on Multihop Ad Hoc Networks: From Theory to Reality*.
- JIANG, X., POLASTRE, J., AND CULLER, D. 2005. Perpetual environmentally powered sensor networks. In *Proceedings of the 4th International Symposium on Information Processing in Sensor Networks*.
- KANSAL, A., POTTER, D., AND SRIVASTAVA, M. B. 2004. Performance aware tasking for environmentally powered sensor networks. In *Proceedings of the Joint International Conference on Measurement and Modeling of Computer Systems*.
- KANSAL, A., HSU, J., ZAHEDI, S., AND SRIVASTAVA, M. B. 2007. Power management in energy harvesting sensor networks. *ACM Trans. Embed. Comput. Syst.*
- KIM, S. 2007. Wireless sensor networks for high frequency sampling. Ph.D dissertation, University of California at Berkeley.
- LANDSIEDEL, O., WEHRLE, K., AND GÖTZ, S. 2005. Accurate prediction of power consumption in sensor networks. In *Proceedings of the 2nd IEEE Workshop on Embedded Networked Sensors*.
- LEVIS, P., PATEL, N., CULLER, D., AND SHENKER, S. 2004. Trickle: A self-regulating algorithm for code propagation and maintenance in wireless sensor networks. In *Proceedings of the 1st Symposium on Networked Systems Design and Implementation*.
- MADDEN, S., FRANKLIN, M. J., HELLERSTEIN, J. M., AND HONG, W. 2002. Tag: A tiny aggregation service for ad-hoc sensor networks. In *Proceedings of the 5th Symposium on Operating Systems Design and Implementation*.
- METEONORM. 2003. Meteonorm. http://www.meteotest.ch/pdf/am/mn_description.pdf.
- MONTENEGRO, G., KUSHALNAGAR, N., HUI, J., AND CULLER, D. 2007. Transmission of ipv6 packets over ieee 802.15.4 networks. <http://tools.ietf.org/html/rfc4944>.
- MOSER, C., BRUNELLI, B., THIELE, L., AND BENINI, L. 2006a. Lazy scheduling for energy harvesting sensor nodes. In *Proceedings of the IFIP Conference from Model-Driven Design to Resource Management for Distributed Embedded Systems*.
- MOSER, C., BRUNELLI, B., THIELE, L., AND BENINI, L. 2006b. Real-time scheduling with regenerative energy. In *Proceedings of the 18th Euromicro Conference on Real-Time Systems*.

- MOSER, C., THIELE, L., BRUNELLI, D., AND BENINI, L. 2007. Adaptive power management in energy harvesting systems. In *Proceedings of the Conference on Design, Automation and Test in Europe*.
- NAHAPETIAN, A., LOMBARDO, P., ACQUAVIVA, A., BENINI, L., AND SARRAFZADEH, M. 2007. Dynamic reconfiguration in sensor networks with regenerative energy sources. In *Proceedings of the Conference on Design, Automation and Test in Europe*.
- NATH, S., GIBBONS, P. B., SESHAN, S., AND ANDERSON, Z. R. 2004. Synopsis diffusion for robust aggregation in sensor networks. In *Proceedings of the 2nd ACM Conference on Embedded Networked Sensor Systems*.
- NSR. 2008. National Solar Radiation Database. http://rredc.nrel.gov/solar/old_data/nsrdb.
- OSTERWALD, R. R., ANDERBERG, A., RUMMEL, S., AND OTTOSON, L. 2002. Degradation analysis of weathered crystalline-silicon pv modules. In *Proceedings of the 29th IEEE Photovoltaic Specialists Conference*.
- PARK, C. AND CHOU, P. H. 2006. Ambimax: Autonomous energy harvesting platform for multi-supply wireless sensor nodes. *IEEE Sen. Ad Hoc Commun. Netw.*
- PARK, S., SAVVIDES, A., AND SRIVASTAVA, M. B. 2000. Sensorsim: A simulation framework for sensor networks. In *Proceedings of the International Workshop on Modeling Analysis and Simulation of Wireless and Mobile Systems*.
- PARK, S., SAVVIDES, A., AND SRIVASTAVA, M. B. 2001. Simulating networks of wireless sensors. In *Proceedings of the Winter Simulation Conference*.
- PETERSON, J. T., FLOWERS, E. C., AND RUDISILL, J. H. 1978. Urban-rural solar radiation and atmospheric turbidity measurements in the los angeles basin. *J. Appl. Meteorol.* 17, 11, 1595–1609.
- PIORNO, J. R., BERGONZINI, C., ATIENZA, D., AND ROSING, T. S. 2009. Prediction and management in energy harvested wireless sensor nodes. In *Proceedings of the 1st International Conference on Wireless Communications, Vehicular Technology, Information Theory and Aerospace & Electronic Systems Technology*.
- POLASTRE, J., HILL, J., AND CULLER, D. 2004. Versatile low power media access for wireless sensor networks. In *Proceedings of the 2nd ACM Conference on Embedded Networked Sensor Systems*.
- POLASTRE, J., SZEWCZYK, R., AND CULLER, D. 2005. Telos: Enabling ultra-low power wireless research. In *Proceedings of the 4th International Symposium on Information Processing in Sensor Networks*.
- PRADHAN, S. S., KUSUMA, J., AND RAMCHANDRAN, K. 2002. Distributed compression in a dense microsensor network. *IEEE Signal Process. Mag.*
- RAGHUNATHAN, V., KANSAL, A., HSU, J., FRIEDMAN, J., AND SRIVASTAVA, M. 2005. Design considerations for solar energy harvesting wireless embedded systems. In *Proceedings of the 4th International Symposium on Information Processing in Sensor Networks*.
- ROBINSON, E. AND VALENTE, R. J. 1982. Atmospheric turbidity over the united states from 1967 to 1976. U.S. Environmental Protection Agency Report 600382076. <http://nepis.epa.gov/Adobe/PDF/~200/5K9J.PDF>.
- SCAGLIONE, A. AND SERVETTO, S. 2002. On the interdependence of routing and data compression in multi-hop sensor networks. In *Proceedings of the 8th Annual International Conference on Mobile Computing and Networking*.
- SHNAYDER, V., HEMPSTEAD, M., CHEN, B., WERNER-ALLEN, G., AND WELSH, M. 2004. Simulating the power consumption of large-scale sensor network applications. In *Proceedings of the 2nd ACM Conference on Embedded Networked Sensor Systems*.
- SIMJEE, F. AND CHOU, P. H. 2006. Everlast: Long-life, supercapacitor-operated wireless sensor node. In *Proceedings of the International Symposium on Low Power Electronics and Design*.
- SIMON, G., VOLGYESI, P., MAROTI, M., AND LEDECZI, A. 2003. Simulation-based optimization of communication protocols for large-scale wireless sensor networks. In *Proceedings of the IEEE Aerospace Conference*.
- SORBER, J., KOSTADINOV, A., GARBER, M., BRENNAN, M., CORNER, M. D., AND BERGER, E. D. 2007. Eon: A language and runtime system for perpetual systems. In *Proceedings of the 5th ACM Conference on Embedded Networked Sensor Systems*.
- SUNDRESH, S., KIM, W., AND AGHA, G. 2004. Sens: A sensor, environment and network simulator. In *Proceedings of the 37th Annual Simulation Symposium*.
- SZEWCZYK, R., MAINWARING, A., POLASTRE, J., ANDERSON, J., AND CULLER, D. 2004. An analysis of a large scale habitat monitoring application. In *Proceedings of the 2nd ACM Conference on Embedded Networked Sensor Systems*.
- TOLLE, G., POLASTRE, J., SZEWCZYK, R., CULLER, D., TURNER, N., TU, K., BURGESS, S., DAWSON, T., BUONADONNA, P., GAY, D., AND HONG, W. 2005. A macroscope in the redwoods. In *Proceedings of the 3rd ACM Conference on Embedded Networked Sensor Systems*.

- VARSHNEY, M., XU, D., SRIVASTAVA, M., AND BAGRODIA, R. 2007. squalnet: A scalable simulation and emulation environment for sensor networks. In *Proceedings of the 7th International Conference on Information Processing in Sensor Networks*.
- VIGORITO, C. M., GANESAN, D., AND BARTO, A. G. 2007. Adaptive control of duty cycling in energy-harvesting wireless sensor networks. *IEEE Sens. Ad Hoc Commun. Netw.*
- WERNER-ALLEN, G., SWIESKOWSKI, P., AND WELSH, M. 2005. Motelab: A wireless sensor network testbed. In *Proceedings of the 4th International Symposium on Information Processing in Sensor Networks*.
- YE, W., HEIDEMANN, J., AND ESTRIN, D. 2004. Medium access control with coordinated adaptive sleeping for wireless sensor networks. *IEEE/ACM Trans. Netw.* 3.
- YE, W., SILVA, F., AND HEIDEMANN, J. 2006. Ultra-low duty cycle mac with scheduled channel polling. In *Proceedings of the 4th ACM Conference on Embedded Networked Sensor Systems*.
- ZHANG, J., ZHOU, G., HUANG, C., SON, S. H., AND STANKOVIC, J. A. 2007. Tmmac: An energy efficient multi-channel mac protocol for ad hoc networks. In *Proceedings of the IEEE International Conference on Communications*.
- ZHANG, P., SADLER, C. M., LYON, S. A., AND MARTONOSI, M. 2004. Hardware design experiences in zebranet. In *Proceedings of the 2nd ACM Conference on Embedded Networked Sensor Systems*.

Received June 2009; revised May 2010, August 2010, January 2011; accepted March 2011